Experimental Research

INTERNATIONAL JOURNAL OF SURGERY

OPEN

3D-bioprinted functional scaffold based on synergistic induction of i-PRF and laponite exerts efficient and personalized bone regeneration via miRNA-mediated TGF-β/Smads signaling

Bojun Cao, PhD[a,b], Kunqi Zhang, PhD[a], Rongtai Zuo, PhD[a], Zhiyang Kang[a], Jieming Lin, PhD[c], Zhixuan Kang[a], Dinghao Luo, PhD[b], Yimin Chai, MD[a], Jia Xu, PhD[a,*], Qinglin Kang, MD[a,*], Shuo Qiu, PhD[a,*]

Background: Limited stem cells, low vascularization efficiency, and weak osteoinductive activity plague the repair and reconstruction of bone defects with cell-free scaffolds.
Methods: Herein, injectable platelet-rich fibrin (i-PRF) was loaded into a alginate methacryloyl (AlgMA)/gelatin methacryloyl (GelMA)-methylcellulose (AGM) bioink system and constructed a porous hydrogel scaffold by 3D bioprinting. The addition of nanosilicate-laponite (Lap) further enhanced this scaffold and synergized with i-PRF to promote efficient and personalized cranial regeneration.
Results: At the biochemical level, Lap significantly enhanced the ability of the scaffold to retard growth factor release, and multiple physiologically proportional growth factors in the scaffold synergistically promoted rapid neoangiogenesis and concomitantly recruited endogenous bone marrow mesenchymal stem cells (BMSCs). More importantly, the bioactive ions released by Lap markedly promoted the proliferation of BMSCs and consistently induced the osteogenic differentiation of BMSCs. At the immunological level, i-PRF-AGM@Lap significantly attenuates the inflammatory response by promoting macrophage M2 polarization. Mechanistically, miRNA sequencing and functional validation experiments demonstrated that bioactive ions released by Lap could synergize with growth factors in i-PRF to promote osteogenic differentiation of BMSCs through the miR-21 and miR-125a-mediated transforming growth factor-β/Smads signaling pathway.
Conclusion: The results of this study provide a new idea for the personalized treatment of bone defects.

Keywords: 3D bioprinting, bone regeneration, i-PRF, personalized treatment

Introduction

The incidence of bone defects caused by trauma, tumors, inflammation, and infection is prevalent and harmful, and their repair and reconstruction remain a pressing problem and research hotspot in the field of orthopedics[1–3]. Autologous bone grafting, considered the "gold standard" for treating bone defects, faces limitations in clinical application due to a constrained donor source and the risk of complications such as infection and fracture due to additional surgical bone extraction; allogeneic bone carries the risk of inducing immune reactions; and artificial bone filling materials generally lack osteogenic induction properties[4–6]. 3D-bioprinted scaffolds offer a promising solution to overcome these limitations and provide the benefits of personalization to meet the needs of anatomical remodeling and functional repair of bone defects[7,8]. However, the development of bioinks with durable osteogenic induction activity

HIGHLIGHTS

- Autologous injectable platelet-rich fibrin (i-PRF) is a key ingredient in bioinks.
- Injectable platelet-rich AlgMA/GelMA-methylcellulose (i-PRF-AGM@Lap) scaffold slowly releases multiple growth factors and bioactive ions to promote rapid vascularization and bone regeneration.
- i-PRF-AGM@Lap regulates bone marrow mesenchymal stem cell osteogenic differentiation through the miR-21 and miR-125a-mediated transforming growth factor-β/Smads signaling pathway.

[a]Shanghai Sixth People's Hospital Affiliated to Shanghai Jiao Tong University School of Medicine, Shanghai, China, [b]Clinical and Translational Research Center for 3D Printing Technology, Shanghai Jiao Tong University School of Medicine, Shanghai, China and [c]Department of Orthopaedic Surgery, Renji Hospital, South Campus, Shanghai Jiao Tong University School of Medicine, Shanghai, China

Bojun Cao, Kunqi Zhang, and Rongtai Zuo contributed equally to this work.

Sponsorships or competing interests that may be relevant to content are disclosed at the end of this article.

*Corresponding author. Address: Shanghai Sixth People's Hospital Affiliated to Shanghai Jiao Tong University School of Medicine, Shanghai, China. Tel.: +86 13955658263 E-mail: ouhsuiq@163.com (S. Qiu); orthokang@sjtu.edu.cn (Q. Kang); xujia0117@sjtu.edu.cn (J. Xu).

International Journal of Surgery (2025) 111:3193–3211

Received 18 January 2025; Accepted 17 February 2025

Supplemental Digital Content is available for this article. Direct URL citations are provided in the HTML and PDF versions of this article on the journal's website, www.lww.com/international-journal-of-surgery..

Published online 3 March 2025

http://dx.doi.org/10.1097/JS9.0000000000002312

and rapid vascularization capabilities is the primary challenge for the application of 3D-bioprinted scaffolds in the clinical treatment of bone defects.

The utilization of autologous stem cells and growth factors to construct bone regenerative bioinks has been widely studied[9,10]. However, stem cells extracted from autologous tissues, such as bone marrow, necessitate extensive *ex vivo* expansion operations, which poses difficulties in clinical translation and regulatory approval. On the other hand, it is evident that a single recombinant growth factor is insufficient to fulfill the requirements for bone defect repair and reconstruction. Moreover, these recombinant growth factors are expensive, are prone to physicochemical instability, and pose a risk of complications such as ectopic ossification and tumors, thereby further restricting their clinical application[11,12]. Therefore, it is important to find an easily clinically translatable, personalized, safe, and effective "factor" that can be encapsulated in 3D-printed bone regeneration scaffolds to regulate endogenous cell recruitment, proliferation, and differentiation. The selection of autologous injectable platelet-rich fibrin (i-PRF) as the primary active ingredient for novel bone regeneration bioinks is an attractive proposition. i-PRF, a second-generation platelet concentrate product after platelet-rich plasma, is prepared by centrifugation of patients' whole blood and is activated to release various growth factors, including transforming growth factor-β (TGF-β), vascular endothelial growth factor (VEGF), and platelet-derived growth factor (PDGF)[13,14]. These factors play a crucial role in promoting angiogenesis, stem cell proliferation and differentiation, and regulation of the immune microenvironment[13,15]. In addition, their ratios closely resemble physiological ratios *in vivo*, enabling better synergy to promote personalized tissue repair. Although previous clinical trials have reported that PRF significantly promotes soft tissue repair, there have been no reports of PRF effectively repairing bone defects, which may be related to the short-term rapid release of growth factors within PRF, which is not temporally sufficient to effectively induce vascularization and osteogenesis[16].

Laponite (Lap), a synthetic magnesium silicate nanoclay, is widely used as a thickening agent in cosmetics but shows significant potential for clinical applications in regenerative medicine[17,18]. Lap is a disk-shaped particle with a diameter of about 25 nm and a thickness of about 1 nm. Featuring a negatively charged surface and positively charged edges, Lap forms robust electrostatic bonds with growth factors, rendering it valuable as a slow-release agent for drugs[19]. Lap can impart shear-thinning properties to bioinks and enhance the mechanical strength of hydrogel scaffolds[20]. In addition, Lap has the capacity to release ions such as Mg^{2+} and Si^{4+}, and these reactive ions have been reported to promote osteogenic differentiation of bone marrow mesenchymal stem cells (BMSCs), but the precise mechanism behind this remains unclear[21,22]. Therefore, the addition of Lap has the potential to enable the most efficient growth factor release from i-PRF-based bone regeneration bioinks and to work with its active ions to achieve a functional fit between rapid vascularization and sustained osteogenic differentiation induction.

Based on the above findings, in the present study, i-PRF-AGM@Lap bioactive ink was constructed by incorporating i-PRF and Lap into the AlgMA/GelMA-methylcellulose (AGM) system in an appropriate ratio, and a high-stiffness multinetwork hydrogel scaffold for skull regeneration was prepared by 3D bioprinting technology (Fig. 1). We observed a significant enhancement in the mechanical strength of i-PRF-based hydrogel scaffolds with the incorporation of Lap. Lap, on the other hand, not only adsorbs growth factors so that the scaffold can sustain the release of growth factors for more than 2 weeks but also sustains the release of bioactive ions, including Mg^{2+} and Si^{4+}. *In vitro* studies demonstrated that i-PRF-AGM@Lap effectively recruited and promoted the proliferation, migration, osteogenic differentiation, and tube formation of rat BMSCs and human umbilical vein endothelial cells (HUVECs). In addition, it promotes macrophage M2 polarization. Mechanistically, we identified and validated a set of miRNAs that are differentially expressed in response to different component classes of hydrogel scaffolds and further demonstrated that reactive ions, such as Mg^{2+} and Si^{4+}, released from Lap can work together with the growth factors in i-PRF to promote miR-21 expression in BMSCs while suppressing miR-205a expression, act together on the TGF-β/Smad signaling pathway by targeting mothers against decapentaplegic homolog 4 (SMAD4) and SMAD7, respectively, and then regulate the fate of BMSC proliferation and osteogenic differentiation. Furthermore, we demonstrated that this biofunctional scaffold promotes rapid vascular ingrowth and significantly accelerates bone regeneration through subcutaneous scaffold implantation experiments and skull defect repair experiments in rats.

Our protocol effectively overcomes the limitations of traditional treatment of bone defects: for autografts, our approach eliminates the need for secondary bone donor sites, thus avoiding donor site morbidity and limited graft availability; for allografts, the autologous nature of blood derivatives ensures immunocompatibility and resolves the risk of chronic inflammation associated with allograft or xeno-materials; and for synthetic bones, such as the commercially available "Bio-Oss," they generally lack biological activity. In contrast, the continuous release of growth factors from the i-PRF-AGM@Lap scaffold enhances osteogenesis and angiogenesis, overcoming the biological inertia of traditional synthetic bone materials. In addition, for "Infuse Bone Graft," a synthetic bone repair material containing recombinant human bone morphogenetic protein-2 (BMP-2), the concentration of growth factors is too high, far exceeding the physiological dose, and it does not have the function of slow-release, which is prone to lead to ectopic ossification[11]. In contrast, the main active ingredient in the i-PRF-AGM@Lap scaffold is autologous PRF, which can slow-release a variety of growth factors close to physiological ratios and dosages, and can synergistically promote bone regeneration. In conclusion, i-PRF-AGM@Lap scaffolds based on i-PRF and Lap have considerable potential to promote personalized bone regeneration

Methods

The work has been reported in line with the Animal Research: Reporting of In Vivo Experiments (ARRIVE) criteria[23].

Extraction and culture of primary bone marrow mesenchymal stem cells from rat

A 4-week-old healthy male Sprague Dawley (SD) rat weighing about 100 g was taken. The femur was isolated from both sides of the rat in a sterile environment, removed, and placed in a sterile Petri dish. The ends of the femur were cut with sterilized

scissors, and the bone marrow fluid was rinsed out from one side of the femur with a 2-mL syringe of complete medium. After repeated rinsing for five times, the bone marrow cytosol was collected and sucked into a 10-mL dish, and then placed in a constant-temperature cell culture incubator for 48 h. The unaffixed cells were carefully removed, and the culture was continued with the addition of a fresh complete medium. Every 3 days, change the fluid and observe the cell growth and fusion. When the cells grew to 90% confluence, they were passaged. Cells from generations 3 to 5 were used for subsequent experiments.

Preparation of i-PRF and i-PRF-AGM@Lap hydrogel bioinks

Under aseptic conditions, 5 mL of fresh blood was withdrawn from the rat heart and then centrifuged at 700 rpm/min for 4 min, and the upper layer of blood was collected to obtain i-PRF.

Dissolve the photoinitiator in 10 mL of deionized water at 50°C for 40 min with shaking and stirring to fully dissolve. Then 0.2 g of AlgMA (1% w/v) and 0.2 g of methylcellulose were added into the photoinitiator solution, and the solution was shaken and stirred for 2 h at 40°C under the condition of avoiding light. Then 1 g of GelMA (5% w/v) was added into the solution, and the solution

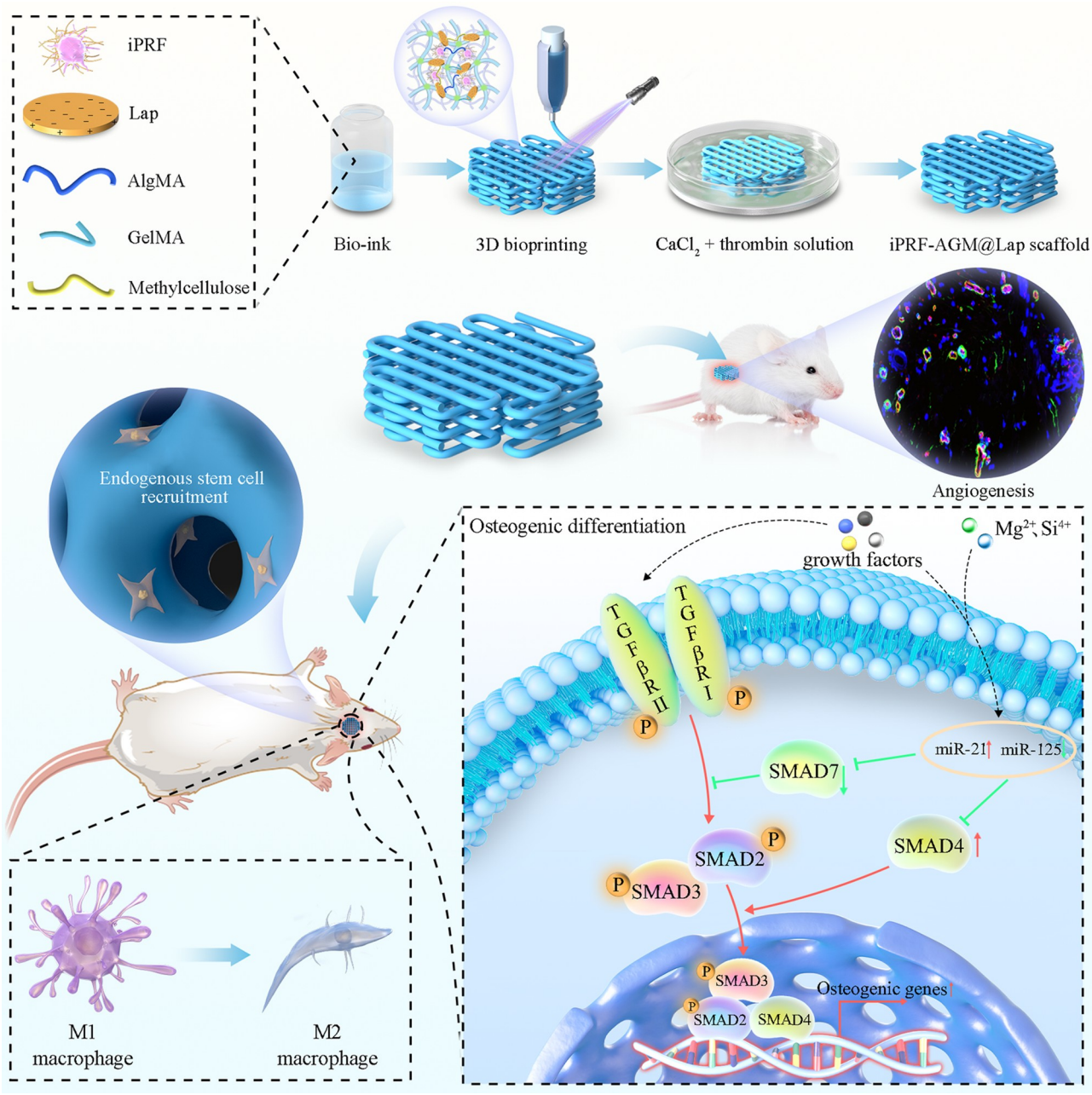

Figure 1. Schematic design and construction of 3D-bioprinted personalized i-PRF-AGM@Lap scaffold. Key components i-PRF and Laponite synergistically induce vascularized bone regeneration.

was shaken and stirred for 40 min at 40ºC under the condition of avoiding light. The solution was then filtered through a 0.22-μm membrane to remove bacteria, and the AlgMA/GelMA/methylcellulose (AGM) hydrogel precursor solution was obtained. The AGM@Lap composite hydrogel precursor containing 1% Lap was constructed by dissolving 0.2 g of Lap particles in 10 mL of deionized water and mixing it with an equal volume of 2% AlgMA/10% GelMA/2% methylcellulose precursor solution. Different volume ratios of i-PRF were added into the AGM@Lap hydrogel precursor to obtain i-PRF-AGM@Lap hydrogel bioink.

3D printing of each group of hydrogel scaffolds

Groups of hydrogel scaffolds were printed using a 3D bioprinter (Bio-Architect; Regenovo, Hangzhou, China). Briefly, the prepared bioinks were loaded into a 250-μm diameter needle cartridge in a sterile environment, and the temperature of the cartridge was adjusted between 15°C and 20°C to achieve stable filament deposition. The temperature of the printing platform was approximately 5°C lower than that of the cylinder, and the printing speed was 10 mm/s with an air compressor pressure of 0.16 MPa. The 3D bioprinting process was performed under an ultraviolet (UV) light source (405 nm, 0.5 W cm^{-2}) for fast curing. Finally, the scaffolds were placed in a 2% (w/v) $CaCl_2$ solution with thrombin dissolved for 10 min to obtain a stable structure.

Morphology and compression modulus of each group of hydrogel scaffolds

The printed scaffolds were placed in a refrigerator at −80°C for 24 h. The scaffolds were taken out and freeze-dried in a freeze-dryer. 48 h later, the samples were removed after observing that the water was almost completely removed from the scaffolds. The samples of each group were gold sputtered and the cross-sections of the lyophilized hydrogels were observed with a scanning electron microscope (SEM, EVO MA10, Germany). The distribution of C, Mg, and Si in the i-PRF-AGM@Lap scaffolds was analyzed using energy dispersive spectroscopy (EDS). The pore size of each group of hydrogels was analyzed and measured using ImageJ software.

Cylindrical hydrogel scaffolds were prepared for uniaxial compression tests. The stress–strain curves of each group of hydrogel scaffolds were obtained using a universal mechanical testing machine (Instron 5969, USA) at a crosshead speed of 5 mm/min. The compression modulus of each group of hydrogels was expressed by the slope of the compression stage from 10% to 20%.

Determination of dissolution rate and degradation properties of hydrogel scaffolds

The initial weight of each group of stents was first weighed and recorded as W_0, then each group of stents was submerged in a 50-mL centrifuge tube filled with phosphate buffered saline (PBS) (PH 7.4), and at set time points (3, 6, 9, 12, and 15 h), they were removed, the surface liquid was wiped off, and the stents were weighed and recorded as W_t. The rate of expansion was calculated using the following formula:

$$\text{Swelling rate } (\%) = (W_t - W_0)/W_0 \times 100\%.$$

To detect the degradation rate (DR) of each group of hydrogel scaffolds, each group of hydrogel scaffolds was degraded by placing the scaffolds in PBS and shaking them with slow oscillations on a shaker at 37°C. The samples were removed at each set time point (4, 8, 12, 16, 20, and 24 days), lyophilized, and weighed (dry weight, W_t). W_0 represents the initial dry weight and the DR of each sample was calculated by using the following formula:

$$\text{DR } (\%) = (W_0 - W_t)/W_0 \times 100\%.$$

Growth factor release assay

The release of several key growth factors from hydrogel scaffolds was measured by enzyme-linked immunosorbent assay (ELISA). Briefly, hydrogel scaffolds are placed in 50-mL centrifuge tubes filled with PBS and placed on a shaker at 37°C. The supernatant from each group of tubes was aspirated at each time point and stored in a refrigerator at −80°C, and then an equal volume of fresh PBS solution was added to each tube. Finally, the concentrations of VEGF, PDGF-BB, IGF-1, and TGF-β were determined using the appropriate ELISA kits according to the method provided by the manufacturer.

Inductively coupled plasma spectrometer tests

To investigate the silicon (Si^{4+}), lithium (Li^{+}), and magnesium (Mg^{2+}) release from the i-PRF-AGM@1%Lap scaffolds, the scaffolds were immersed in PBS (pH 7.4) for 1, 5, 10, 14, 21, 28, 35, and 42 days. The solution was collected at each time point and the ion contents were determined by using an inductively coupled plasma source spectrometer (Prodigy-ICP, USA).

Cell viability assay of the scaffolds

Live/dead cell staining and Cell Counting Kit 8 (CCK-8) assays were performed on these scaffolds in two ways. First, the cells were incubated with the extracts of each group of scaffolds for 1, 3, and 5 days and then the CCK-8 detection reagent was added, taking care that the CCK-8 reagent should be added along the wall of the wells as much as possible to avoid air bubbles, which could affect the readings. After adding the CCK-8 reagent, place the plate in the incubator. After the addition of CCK-8 reagent, the plate was placed in the incubator and incubated for about 1 h, then the plate was taken out and the absorbance at 450 nm was measured using an enzyme marker. In addition, the cells were stained with PI and calcein-acetoxymethyl ester (AM) and then observed with an inverted fluorescence microscope. The second way was to encapsulate the cells in bioink for printing the scaffolds and culture for 1 and 3 days before CCK-8 assay and live/dead cell staining.

Western blot analysis

Proteins were isolated from rat BMSCs, and Western blotting was performed as described previously. Antibodies against β-actin (Abcam), COL1 (Abcam), Runx2 (Abcam), proliferating cell nuclear antigen (PCNA) (cell signaling), cyclin D1 (Abcam), Smad 2 (cell signaling), phosphorylated Smad 2 (cell signaling), Smad 3 (cell signaling), phosphorylated Smad 3 (cell signaling), Smad 7 (Abcam), and Smad 4 (Abcam) were used for immunoblotting. Images were captured by an ImageQuant LAS4000 Imaging Station (GE), and band densities were quantified by using ImageQuant TL software (GE).

Quantitative real-time polymerase chain reaction analysis

Briefly, for RAW264.7, total RNA from RAW264.7 was isolated with TRIzol reagent (Invitrogen). The primer sequences were

inducible nitric oxide synthase (iNOS): forward 5′-(GTTCTCAG CCCAACAATACAAGA)-3′ and reverse 5′-(GTGGACGGGT CGATGTCAC)-3′; chemokine C-C-motif receptor 7 (CCR7): forward 5′-(GAGGCTCAAGACCATGACGGA)-3′ and reverse 5′-(ATCCAGGACTTGGCTTCGCT)-3′; Arg1: forward 5′-(GGT GGCAGAGGTCCAGAAGAA)-3′ and reverse 5′-(CCCATGCA GATTCCCAGAGC)-3′; and CD206: forward 5′-(CTCTGTTCA GCTATTGGACGC)-3′ and reverse 5′-(CGGAATTTCTGGGAT TCAGCTTC)-3′. Glyceraldehyde-3-phosphate dehydrogenase (GAPDH) was used as an internal control for expression normalization.

For BMSC, total RNA from rat BMSCs was isolated with TRIzol reagent (Invitrogen). Polymerase chain reaction (PCR) analysis of miRNAs was performed using the following primers: miR-21-5p (forward: ACACTCCAGCTGGGTAGCTTATCAGACTGA; reverse: CTCAACTGGTGTCGTGGAGTCGGCAATTCAGTT GAGTCAACATC), miR-199a-5p (forward: ACACTCCAGCTG GGCCCAGTGTTCAGACTAC; reverse: CTCAACTGGTGTCG TGGAGTCGGCAATCAGTTGAGGAACAGGT), miR-146b-5p (forward: ACACTCCAGCTGGGTGAGAACTGAATTCCATA; reverse: CTCAACTGGTGTCGTGGAGTCGGCAATTCAGTT GAGACAGCCTA), miR-204-5p (forward: ACACTCCAGCTG GGTTCCCTTTGTCATCCT; reverse: CTCAACTGGTGTCGT GGAGTCGGCAATTCAGTTGAGAGGCATAG), miR-125a-5p (forward: ACACTCCAGCTGGGTCCCTGAGACCCTTTAAC; reverse: CTCAACTGGTGTCGTGGAGTCGGCAATTCAGTT GAGTCACAGGT), and U6 (forward: CTCGCTTCGGCAGC ACA; reverse: AACGCTTCACGAATTTGCGT). The expression level of U6 was used as an endogenous control.

Osteogenic differentiation assay

Each group of scaffolds was immersed in serum-free medium for 3 days and then mixed with BMSC standard osteogenic differentiation induction medium (DMEM/F-12, containing 100 nM dexamethasone, 10 mM β-glycerophosphate, and 50 μg mL^{-1} L-ascorbic acid) at a volume of 1:1 to make a mixed induction medium. BMSCs were inoculated into each well of a 24-well plate at a density of 4×10^4 cells/well, and when the cell growth reached 70% fusion, the medium was aspirated and was washed carefully with PBS three times in each well. When the cell growth reached 70% confluence, the medium in the wells was aspirated and washed carefully with PBS three times, 500 μL of preconfigured osteogenic induction medium was added to each well, and then the well plates were placed in a cell culture incubator at 37°C for incubation, and the medium was changed every 2–3 days. Alizarin red staining was carried out on the cells in each well after 14 and 21 days of induction.

Cell scratch assay

Seven lines were drawn parallel to the bottom of a six-well plate with a marker pen. HUVECs or rat BMSCs were inoculated into each well at a density of 1.5×10^5 cells/well. When the cells reached 90% confluence, alpha minimal essential medium (α-MEM) medium containing 0.5% fetal bovine serum (FBS) was used for starvation treatment for 24 h. A 200-μL sterile lance tip was used to make scratches on the bottom of the plate in the perpendicular direction of the parallel marker lines, and then the cells scraped off by the lance tip were carefully washed with PBS solution. The scaffold extracts of each group were added to the well plates of each group separately. Photographs were taken under a microscope immediately (0 h) and after 24 h of incubation with the mixed osteogenic medium, and the migration data of cells in each group were counted using Image J software.

Subcutaneous scaffold implantation on the back of rats

After the SD rats were fully anesthetized, the backs of the rats were dehairing, disinfected with iodophor, and then disinfected three times with 75% alcohol. Using autoclaved scissors and forceps, a 1-cm-long skin incision was made on each side of the rat's back, two subcutaneous pouches were obtained by bluntly separating the skin, and the scaffolds were carefully implanted in each of the subcutaneous pouches of the rat. The area was wiped with 75% alcohol and then exposed. The rats were placed on a thermostatic water pad and waited for the rats to wake up, and then housed in individual cages and fed with the usual diet. Two weeks after the operation, the rats were executed by overdose anesthesia, the skin on the back of the rats was carefully cut open to separate the stent from the surrounding tissue envelope, and then the specimens were removed.

Dual-luciferase reporter assay

To construct the Smad 7 3′-untranslated region (3′-UTR) reporter, a fragment of the Smad 7 3′-UTR, including a putative miR-21-binding site, was amplified by PCR with primers containing Pme I and Sac I restriction enzyme sites and then inserted into the 3′ end of the firefly luciferase gene in the pMir-report vector (Ambion, Applied Biosystems). A mutation of the miR-21 seeding site was introduced into the pMir-report by a QuickChange Site-Directed Mutagenesis Kit (Agilent Technologies) according to the manufacturer's instructions. The level of luciferase activity was then assessed by measuring the activity of firefly luciferase relative to that of the control (TK Renilla) according to the manufacturer's instructions. A Smad 4 3′-UTR reporter gene was constructed in a similar method.

Construction of rat skull defect model

Eight-week-old male SD rats ($n = 80$) were randomly and equally assigned to the control blank group and the following treatment groups: the AGM group, the i-PRF-AGM group, and the i-PRF-AGM@Lap group, and each group was randomly and equally divided into a 4-week-time treatment group and an 8-week-time treatment group. The rats were anesthetized and a 5-mm diameter bone defect was constructed at the top of the skull using a dental drill, followed by implantation of a hydrogel scaffold. Micro-CT analysis was performed to observe the degree of bone repair of different scaffolds and the ratio of new bone volume (BV) to tissue volume (TV) (BV/TV) was analyzed by CT-Analyzer software.

Histological staining

Rats in each group were anesthetized and sacrificed at 4 and 8 weeks postoperatively to collect rat skull samples. Specimens were fixed in paraformaldehyde solution for 48 h and then decalcified. The decalcified skull specimens were then embedded and sectioned, followed by hematoxylin and eosin (H&E), Masson's trichrome, and Goldner's trichrome staining.

Statistical analysis

At least three times each experiment was repeated independently with similar results. Results are expressed as the mean ± standard deviation, and statistical analysis was performed using GraphPad Prism 8.0. One-way analysis of variance followed by Tukey's multiple comparison tests was applied for comparisons between multiple groups, and Student's *t*-tests were applied for comparing differences between two groups. A value of $P < 0.05$ was considered statistically significant.

Results

Fabrication and characterization of bioink and scaffolds

In order to construct bioinks with good biocompatibility and printability, we constructed AGM basic hydrogel bioink on the basis of our previous research[24], and tested them by a triaxial bioprinter system and found that AGM could be stabilized out of filaments, and the cylindrical scaffolds could be cured and shaped rapidly under the cross-linking effect of UV light (Supplementary Fig. S1, http://links.lww.com/JS9/D984). Then the AGM hydrogel precursor solution was mixed with different concentrations of i-PRF to prepare different concentrations of i-PRF-AGM hydrogel scaffolds. By CCK-8 assay, it was found that AGM scaffolds containing i-PRF significantly promoted BMSC proliferation after 1 day of culture, with the 10% i-PRF-AGM and 20% i-PRF-AGM groups promoting cell proliferation significantly more than the other groups. After 3 and 5 days of culture, the 10% i-PRF-AGM group showed the best pro-proliferation effect (Supplementary Fig. S2, http://links.lww.com/JS9/D984). Based on this, we used a 10% i-PRF-AGM formulation in subsequent experiments. To further enhance the performance of the i-PRF-based hydrogel scaffolds, Lap was added to the i-PRF-AGM bioinks to prepare i-PRF-AGM@Lap scaffolds, and the scaffolds were fabricated as shown in Fig. 2A. Lap is a shear thickening agent, and Lap enhances the shear-thinning behavior of the bioinks in a concentration-dependent manner, and the low viscosity under high shear ensured the smooth extrusion, while the high enough viscosity after shear ensures the moldability after printing (Fig. 2D). It was observed by optical microscopy that the bioinks with 1% and 2% Lap concentration showed better printing accuracy than the other groups of inks with low Lap concentration and without Lap (Fig. 2B). The internal morphology of the lyophilized AGM, i-PRF-AGM, i-PRF-AGM@0.5% Lap, i-PRF-AGM@1%Lap, and i-PRF-AGM@2%Lap scaffolds was examined by SEM. As shown in Fig. 2B, the SEM images of each group of scaffolds showed interconnected porous microstructures.

Compared with the AGM and i-PRF-AGM groups, the Lap-containing i-PRF-AGM scaffolds showed a gradual increase in the number of micropores and a gradual decrease in the pore size with the increase in the Lap concentration (Fig. 2B, F), which indicated that the cross-linking degree of the hydrogel scaffolds was enhanced by the incorporation of Lap nanoparticles. In addition, the uniform distribution of Mg and Si elements in the i-PRF-AGM@Lap scaffolds was found by EDS detection, suggesting that the Lap nanoparticles were homogeneously added to the i-PRF-AGM bioinks (Fig. 2C).

In order to clarify the effect of Lap on the mechanical properties of each group of scaffolds, we examined the compressive modulus of each group of scaffolds (Fig. 2E). The compressive modulus values of AGM and i-PRF-AGM scaffolds were 78.20 ± 4.85 and 131.23 ± 7.38 kPa, respectively; the compressive modulus values of the scaffolds with the addition of Lap at concentrations of 0.5%, 1%, and 2% reached 166.33 ± 10.49, 203.83 ± 9.78, and 218.07 ± 16.42 kPa, respectively; and the results proved that the addition of Lap could significantly enhance the mechanical strength of the scaffold.

The swelling and degradation properties of hydrogel scaffolds are critical for maintaining their stability and promoting tissue regeneration[25,26]. As shown in the swelling curves (Fig. 2G), the swelling rates of AGM, i-PRF-AGM, i-PRF-AGM@0.5%Lap, i-PRF-AGM@1%Lap, and i-PRF-AGM@2%Lap scaffolds were 39.90 ± 3.02%, 30.97 ± 2.55%, 21.13 ± 1.42%, 18.90 ± 0.82%, and 17.43 ± 1.29%, respectively, after 15 h of immersion in PBS. The swelling rate of Lap-doped scaffolds decreased significantly with increasing Lap content. In addition to possessing good swelling properties, the i-PRF-AGM@Lap scaffolds exhibited lower DRs compared to the AGM and i-PRF-AGM groups, and the scaffold DR gradually slowed down with increasing Lap content (Fig. 2H). The high cross-linking density of Lap-containing hydrogel scaffolds resulted in moderate DRs and low swelling compared with the AGM and i-PRF-AGM scaffold groups, and this stability was favorable for promoting tissue regeneration.

Cell viability and growth factor release assay of scaffold in vitro

To clarify the effect of the concentration of Lap in the scaffolds on cell viability, we performed live/dead cell staining and CCK-8 assay on these scaffolds in two ways. First, we used the extracts from each group of scaffolds for the induction culture of BMSCs, and the results showed that the number of cells in each group increased with the incubation time (Fig. 3A, B). None of the scaffolds showed significant cell growth inhibition except for the 2% Lap concentration scaffold group. Western blot assay results further showed that the expression of PCNA and cyclin D1 proteins was significantly increased in the i-PRF-AGM group and the i-PRF-AGM@Lap group except for the 2% Lap concentration, as compared to the scaffolds in the AGM group (Fig. 3C–E). Next, we encapsulated the cells in bioink for printing scaffolds and cultured them in 3D. The results of live/dead cell staining and CCK-8 assay were similar to the former (Fig. 3F, G). In summary, i-PRF in the scaffolds significantly promoted BMSC proliferation, and the addition of Lap further promoted cell proliferation when the concentration of Lap was lower than 2%. Based on the results of the bioprinting test and cell viability assay of the scaffolds, we selected the i-PRF-AGM@Lap scaffolds with 1% Lap for subsequent studies.

During normal fracture healing, VEGF expression peaks around day 10 and then declines, suggesting the need for a delivery system that supports early VEGF release. Activated PRF releases a variety of key osteogenic and angiogenic growth factors and has been used in the clinical treatment of fractures, osteoarthritis, and difficult-to-heal wounds[13]. However, the early burst release of growth factors in PRF severely limits its therapeutic efficacy. Previous findings have shown that pure PRF gels burst release the vast majority of growth factors within 3 days[13,14]. In order to clarify whether i-PRF-AGM and i-PRF-AGM@Lap could play a role in slowing down the release of

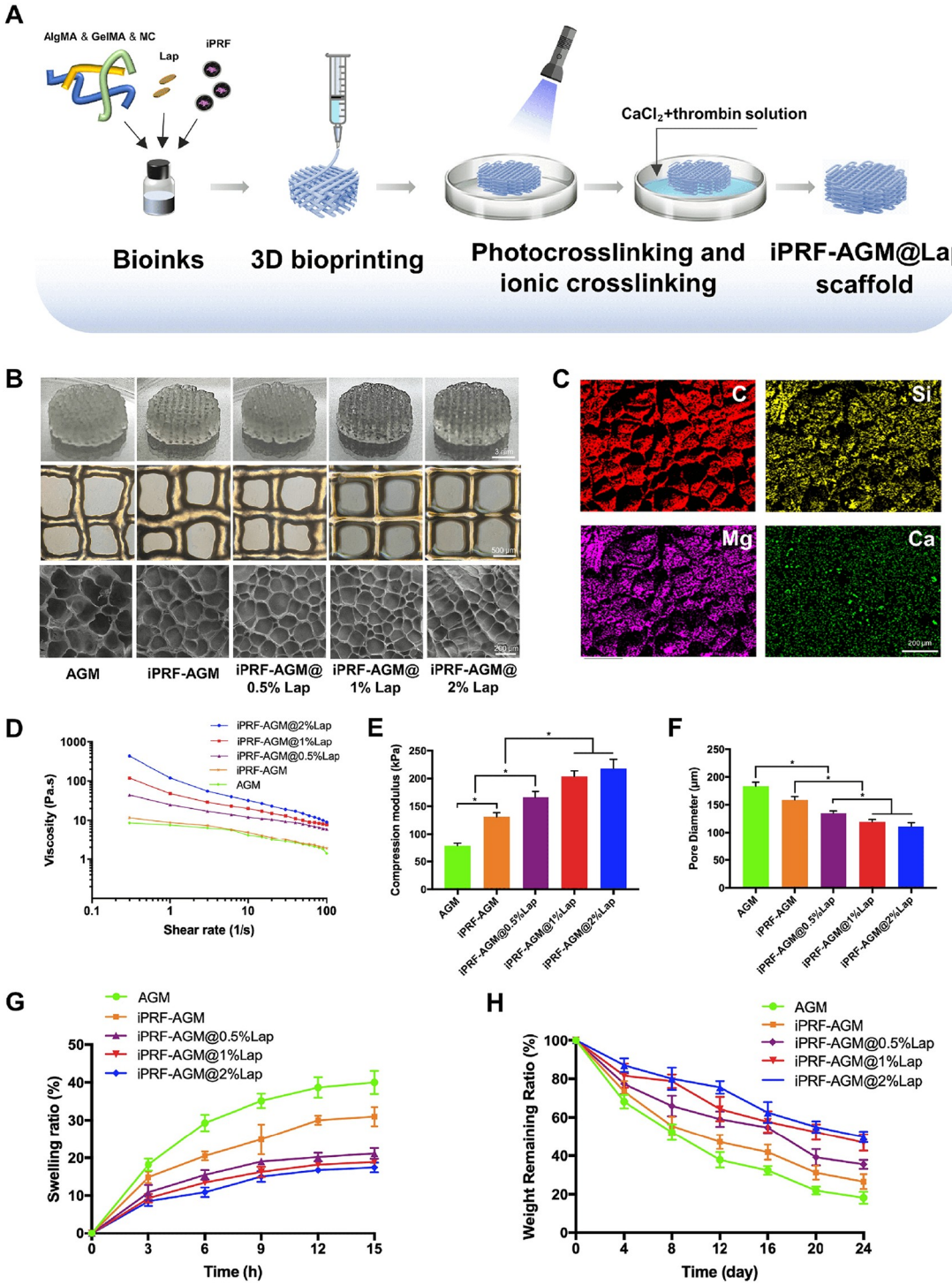

Figure 2. Characterization of each group of scaffolds. (A) Schematic of the fabrication of i-PRF-AGM@Lap scaffolds. (B) Representative images and SEM inspection images of AGM, i-PRF-AGM, i-PRF-AGM@0.5%Lap, i-PRF-AGM@1%Lap, and i-PRF-AGM@2%Lap scaffolds. (C) X-ray energy dispersion spectra of i-PRF-AGM@1%Lap scaffolds: C (red), Si (yellow), Mg (purple), and Ca (green). (D) Viscosity of different bioinks as a function of shear rate at 25°C. (E) Compression modulus of different scaffolds. (F) Pore size of different scaffolds. (G, H) Swelling and degradation rates of different scaffolds. Statistical analysis was performed using one-way analysis of variance and Tukey's method ($n = 3$ independent experiments, $^*P < 0.05$). AGM, AlgMA/GelMA-methylcellulose i-PRF, injectable platelet-rich fibrin; Lap, laponite; SEM, scanning electron microscope.

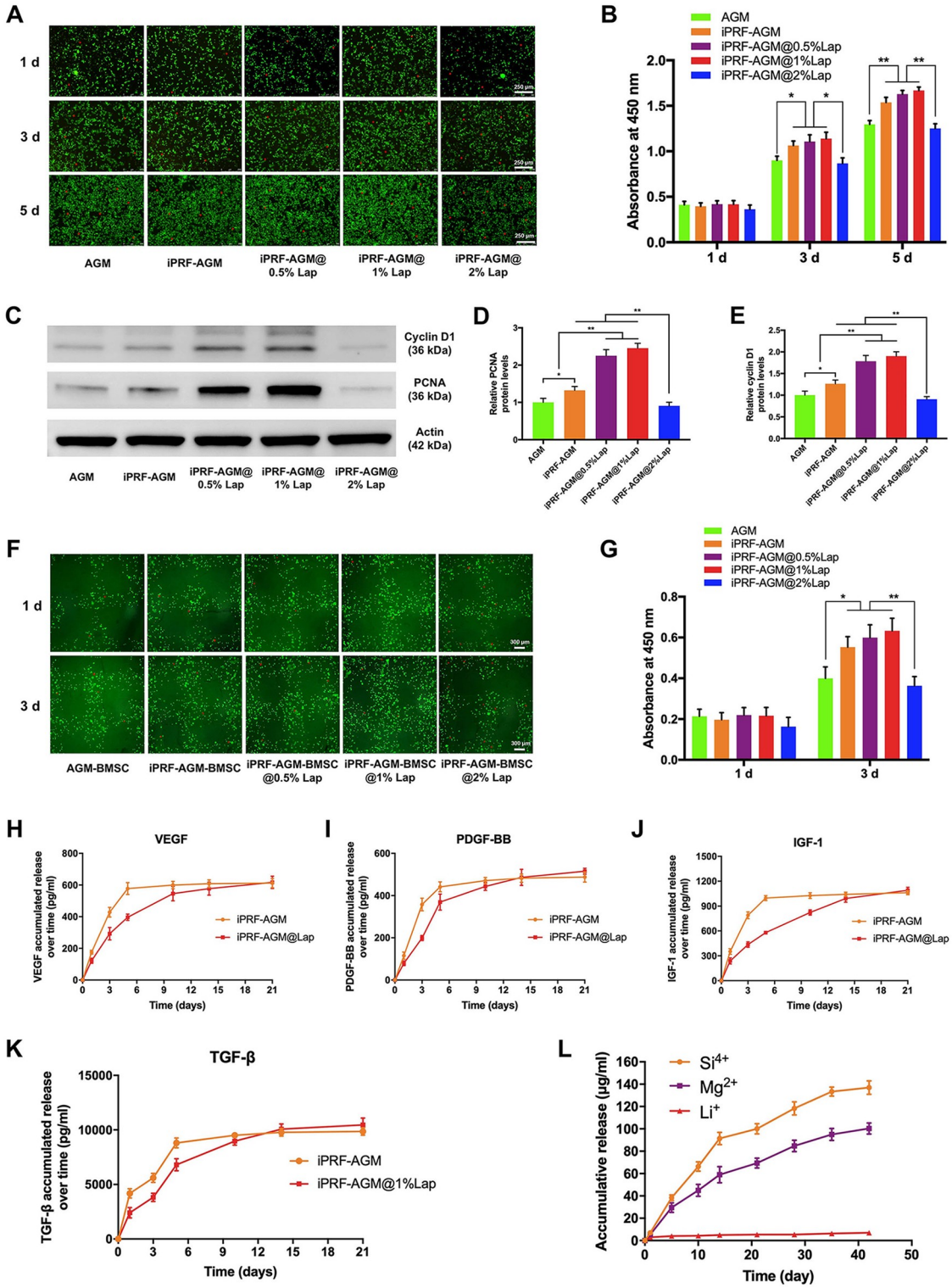

Figure 3. Biocompatibility and growth factor release assay of each group of scaffolds. (A) Live/dead staining assay of cells cultured in extracts of each group of scaffolds. (B) CCK-8 assay for proliferation of cells cultured in extracts of each group of scaffolds. (C–E) Cyclin D1 and PCNA protein expression in BMSC cultured in extracts of each group of scaffolds. (F) BMSCs were encapsulated in bioink to print the scaffold and cultured in 3D for 1 and 3 days for live/dead cell staining. (G) CCK-8 detected the proliferation of cells in the scaffolds in each group. (H–K) Time-dependent release profiles of TGF-β, VEGF, PDGF-BB, and IGF-1 in the two groups of scaffolds. (L) *In vitro* release assay of Si, Mg, and Li ions in i-PRF-AGM@Lap scaffolds. Statistical analyses were performed using one-way analysis of variance and Tukey's method ($n = 3$ independent experiments, $^{*}P < 0.05$ and $^{**}P < 0.01$). AGM, AlgMA/GelMA-methylcellulose; BMSC, bone marrow mesenchymal stem cell; CCK-8, Cell Counting Kit 8; i-PRF, injectable platelet-rich fibrin; Lap, laponite; PCNA, proliferating cell nuclear antigen; PDGF-BB, platelet-derived growth factor-BB; TGF-β, transforming growth factor-β; VEGF, vascular endothelial growth factor.

growth factors, we examined the release kinetics of TGF-β, VEGF, PDGF-BB, and IGF-1 from the two groups of scaffolds by ELISA. As shown in Fig. 3H–K, compared with the weaker slow-release effect in the i-PRF-AGM group, i-PRF-AGM@Lap demonstrated the ability to continuously release growth factors for about 2 weeks, and the majority of its released growth factors were released within 10 days, which is favorable for strongly promoting neovascularization in the early stage of bone defects. Due to the incorporation of Lap in the bioink, the i-PRF-AGM@Lap scaffold can also slow-release active ions Mg^{2+} and Si^{4+}. As shown in Fig. 2L, Si^{4+} ions and Mg^{2+} ions can be released continuously for more than 40 days, and their ionic concentrations are reported to be in the range that can effectively promote bone defect repair according to previous studies[27].

Effects of i-PRF-AGM@Lap scaffold on BMSC recruitment, migration, and osteogenic differentiation

It would be valuable if the i-PRF-AGM@Lap scaffold could actively recruit endogenous BMSC. We incubated bone marrow cell suspensions from rat femurs with each group of scaffolds for 10 days and then rinsed the scaffolds sufficiently to remove unadhered cells, followed by staining of adhered BMSC with F-actin and cell surface glycoprotein (CD44). i-PRF-AGM@Lap was found to have the strongest ability to recruit BMSC by observing the intensity of CD44 staining and cell morphology, and the adherent cells had a typical shuttle shape morphology and higher spreading area (Fig. 4A, B, Supplementary Fig. S3, http://links.lww.com/JS9/D984). Next, it was found by Transwell assay that i-PRF-AGM and i-PRF-AGM@Lap scaffolds significantly promoted the migration of rat BMSC (Fig. 4C–E), which was further verified in the cell scratch assay test (Fig. 4F, G).

To investigate the effect of the scaffolds on the osteogenic differentiation of BMSCs, the mixed culture medium prepared from the scaffold extracts of each group was used to induce BMSC, and alkaline phosphatase (ALP) staining was performed on the cells of each group after 7 days. The results showed that the i-PRF-AGM and i-PRF-AGM@Lap groups significantly promoted the osteogenic differentiation of BMSCs compared to the AGM and blank control groups. In addition, the proportion of ALP-stained positive cells in the i-PRF-AGM@Lap group was significantly higher than that in the i-PRF-AGM group. Similarly, after 14 days of culture, alizarin red staining and quantitative analysis of BMSCs from each group showed that the i-PRF-AGM group produced a large number of mineralized nodules, significantly more than the AGM and blank control groups, while the i-PRF-AGM@Lap group produced significantly more mineralized nodules than the i-PRF-AGM group (Fig. 4J, K). This difference between groups was even more significant after 21 days of culture. Furthermore, the expression of Runt-related transcription factor 2 (Runx2), an osteogenesis-related marker protein, and Collagen I (COL1) were examined by Western blot in BMSC cultured on scaffolds in each group. The results showed that the expression of Runx2 and COL1 was significantly promoted in the i-PRF-AGM and i-PRF-AGM@Lap groups, and the expression of both proteins was significantly higher in the i-PRF-AGM@Lap group than in the i-PRF-AGM group (Fig. 4L–N). These results showed that the addition of i-PRF could confer osteoinductive activity to the scaffolds, and the further addition of Lap significantly enhanced this function.

Effect of i-PRF-AGM@Lap scaffold on angiogenesis and macrophage polarization

The effect of the extracts from each scaffold group on HUVEC proliferation was detected by CCK-8, and the results showed that the i-PRF-AGM and i-PRF-AGM@Lap groups significantly promoted HUVEC proliferation compared with the AGM and blank control groups (Fig. 5A). Scratch assay and Transwell assay together showed that i-PRF-AGM and i-PRF-AGM@Lap significantly promoted HUVEC migration compared with the other two groups (Fig. 5B–E). In addition, the effect of each scaffold group on HUVEC *in vitro* tube formation was investigated using a tubule formation assay. We directly implanted HUVECs on the surface of each group of hydrogels without the use of special matrix gels. After 6 h of incubation, no significant tubule formation was observed in the AGM hydrogel group and the blank group, whereas a large number of tubules were observed on the surface of the hydrogels in the i-PRF-AGM and i-PRF-AGM@Lap groups (Fig. 5F, G). Furthermore, we subcutaneously implanted the scaffolds of each group on the back of rats to evaluate the vascularization effect of the scaffolds *in vivo* (Supplementary Fig. S4, http://links.lww.com/JS9/D984). After 2 weeks of implantation, we found by immunofluorescence staining that only a small amount of angiogenesis was observed in the AGM group, whereas a large number of mature blood vessels stained positively for α-smooth muscle actin (α-SMA) and CD31 were observed in both the i-PRF-AGM and i-PRF-AGM@Lap groups, and the number of neovasculature in the i-PRF-AGM@Lap group was significantly greater than that in the i-PRF-AGM group (Supplementary Fig. S4, http://links.lww.com/JS9/D984). These results demonstrated the potential pro-angiogenic properties of the i-PRF-AGM@Lap scaffold.

To determine the effect of the scaffold on macrophage polarization, we cultured RAW264.7 cells on each group of hydrogels. The expression of iNOS and CCR7 (M1 markers) genes was found to be significantly decreased in cells cultured on i-PRF-AGM and i-PRF-AGM@Lap hydrogels by quantitative PCR (q-PCR) assay (Fig. 5H, I), whereas the expression of Arg1 and CD206 (M2 markers) genes was significantly increased compared to AGM and blank control groups (Fig. 5J, K). Furthermore, the immunofluorescence staining results of iNOS and Arg1 were consistent with the qPCR results (Fig. 5L, M). The above results indicated that both i-PRF-AGM and i-PRF-AGM@Lap could promote macrophage polarization to M2 type.

Synergistic regulation of miRNA expression by i-PRF and Lap in i-PRF-AGM@Lap scaffolds to promote BMSC osteogenic differentiation

miRNAs play an important role in mediating the regulation of MSC fate by the biophysical and biochemical microenvironments, including proliferation, osteogenesis, and lipogenesis[28–30]. To clarify whether miRNA expression is different in each scaffold group, we cultured BMSC on three scaffolds, AGM, i-PRF-AGM, and i-PRF-AGM@Lap, and performed miRNA sequencing on the three groups of cells after 48 h. As shown in Fig. 6A, there were 122 differentially expressed genes in i-PRF-AGM vs. AGM, 74 differentially expressed genes in i-PRF-AGM@Lap vs. AGM, and 8 differentially expressed genes in i-PRF-AGM@Lap vs. i-PRF-AGM@Lap. The volcano and heat maps of differentially expressed gene analysis further showed that 46 genes were

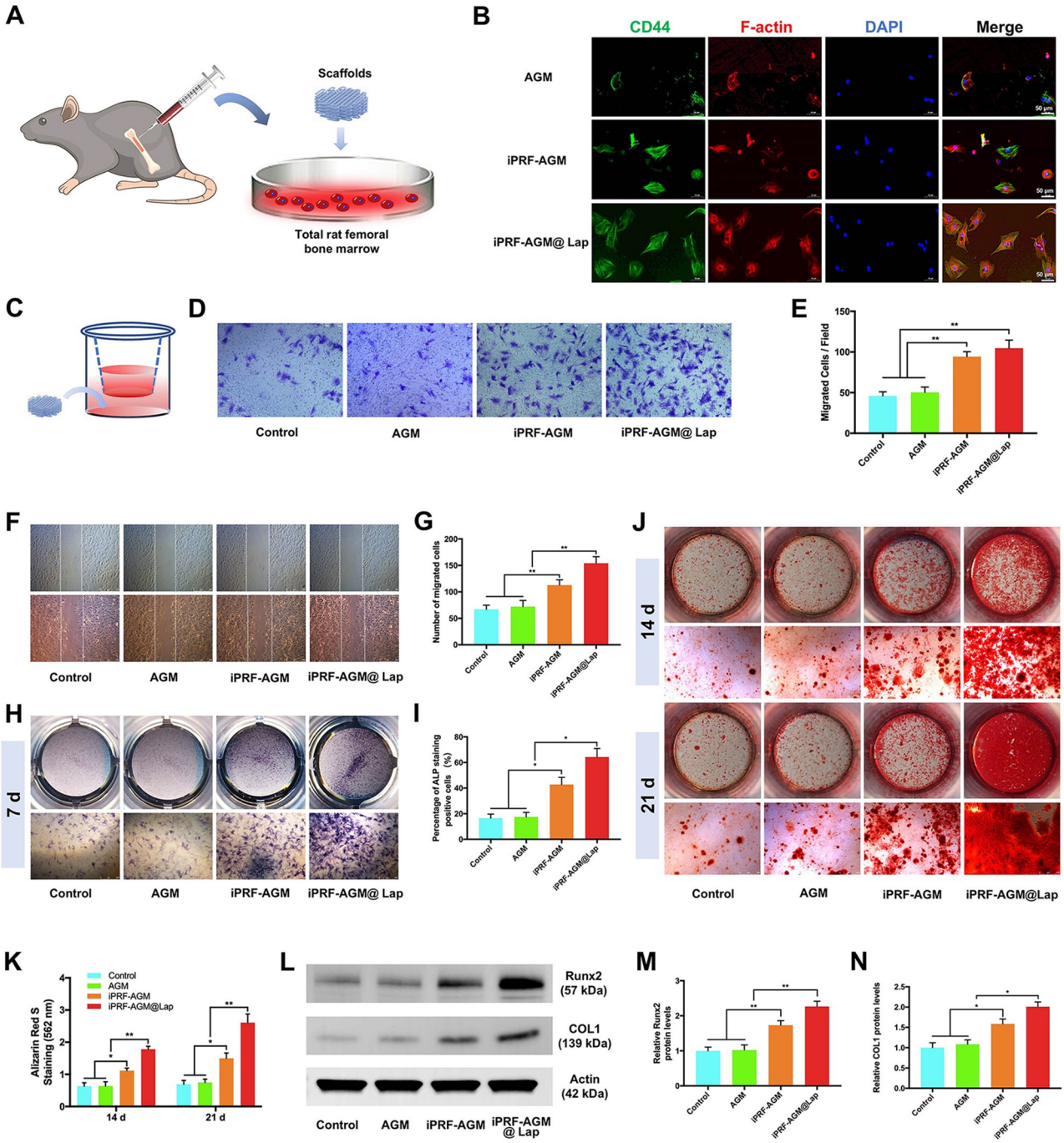

Figure 4. Effect of each group of scaffolds on BMSC recruitment, migration, and osteogenic differentiation. (A) Schematic diagram of each group of scaffolds placed into rat femur bone marrow fluid and cultured for 5 days to detect BMSC recruitment. (B) Immunofluorescence staining of CD44 and F-actin on BMSC adhering to each group of scaffolds. (C–E) The effect of each group of scaffolds on BMSC migration was detected by Transwell assay. (F, G) The effect of extracts from each group of scaffolds on BMSC migration was detected by cell scratch assay. (H, I) ALP staining and quantitative analysis after 7 days of culture. (J, K) Alizarin red-S staining and quantitative analysis after 14 and 21 days of culture, respectively. (L–N) Representative Western blot images and quantitative analysis of Runx2 and COL1 protein expression in BMSC. Statistical analyses were performed using one-way analysis of variance and Tukey's method ($n = 3$ independent experiments, $^{*}P < 0.05$ and $^{**}P < 0.01$). AGM, AlgMA/GelMA-methylcellulose; BMSC, bone marrow mesenchymal stem cell; i-PRF, injectable platelet-rich fibrin; Lap, laponite; ALP, alkaline phosphatase.

upregulated and 28 genes were downregulated in i-PRF-AGM vs. AGM, and 77 genes were upregulated, and 45 genes were downregulated in i-PRF-AGM vs. AGM (Fig. 6B–E). Gene ontology (GO) functional analysis was then performed on the target genes of these miRNAs using TopGO software, and the target genes in i-PRF-AGM vs. AGM and i-PRF-AGM@Lap vs. AGM were sequentially enriched in extracellular matrix (ECM), cell migration, cell adhesion, angiogenesis, and ossification (Supplementary

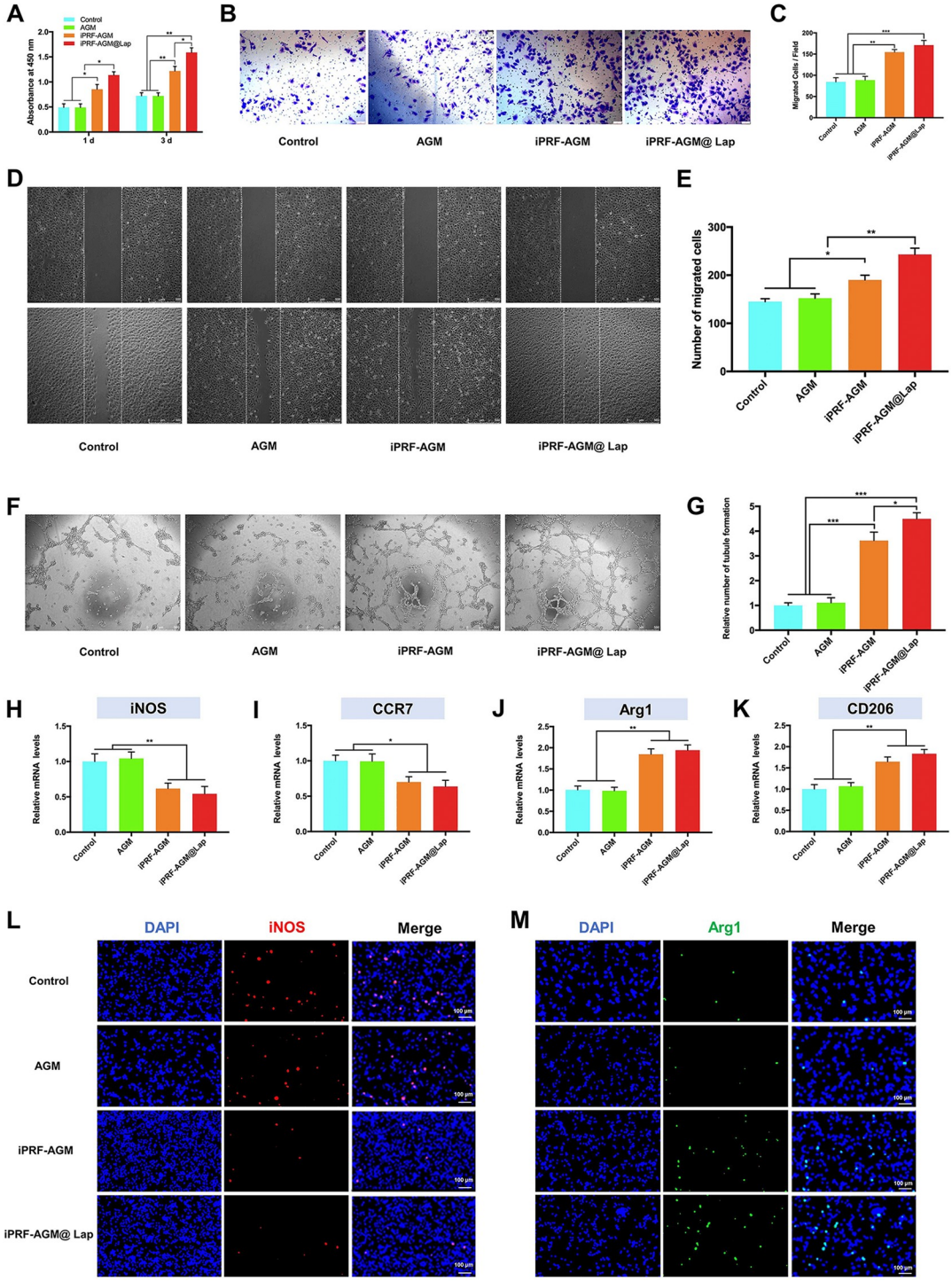

Figure 5. Effect of each group of scaffolds on angiogenesis and macrophage polarization. (A) Effect of extracts from each group of scaffolds on HUVEC proliferation detected by CCK-8. (B, C) Effect of each group of scaffolds on HUVEC migration detected by Transwell assay. (D, E) Effect of extracts of each group of scaffolds on HUVEC migration detected by cell scratch assay. (F) Representative images of the effect of each group of scaffolds on HUVEC tubule formation *in vitro*. (G) Relative number of tubules formed. (H, I) Results of q-PCR assay (CCR7 and iNOS) of each group of scaffolds on the expression of genes related to M1 polarization in macrophages at the *in vitro* level. (J, K) Results of q-PCR detection of M2 polarization-related gene expression (CD206 and Arg1). (L) Immunofluorescence staining of iNOS protein in each group (red). (M) Immunofluorescence staining of Arg1 protein in each group (green). Statistical analyses were performed using one-way analysis of variance and Tukey's method (n = 3 independent experiments, $^{*}P < 0.05$ and $^{**}P < 0.01$). AGM, alginate/gelatin-AlgMA/GelMA-methylcellulose; CCK-8, Cell Counting Kit 8; i-PRF, injectable platelet-rich fibrin; Lap, laponite; PCNA, proliferating cell nuclear antigen; q-PCR, quantitative polymerase chain reaction; HUVEC, human umbilical vein endothelial cell; iNOS, inducible nitric oxide synthase.

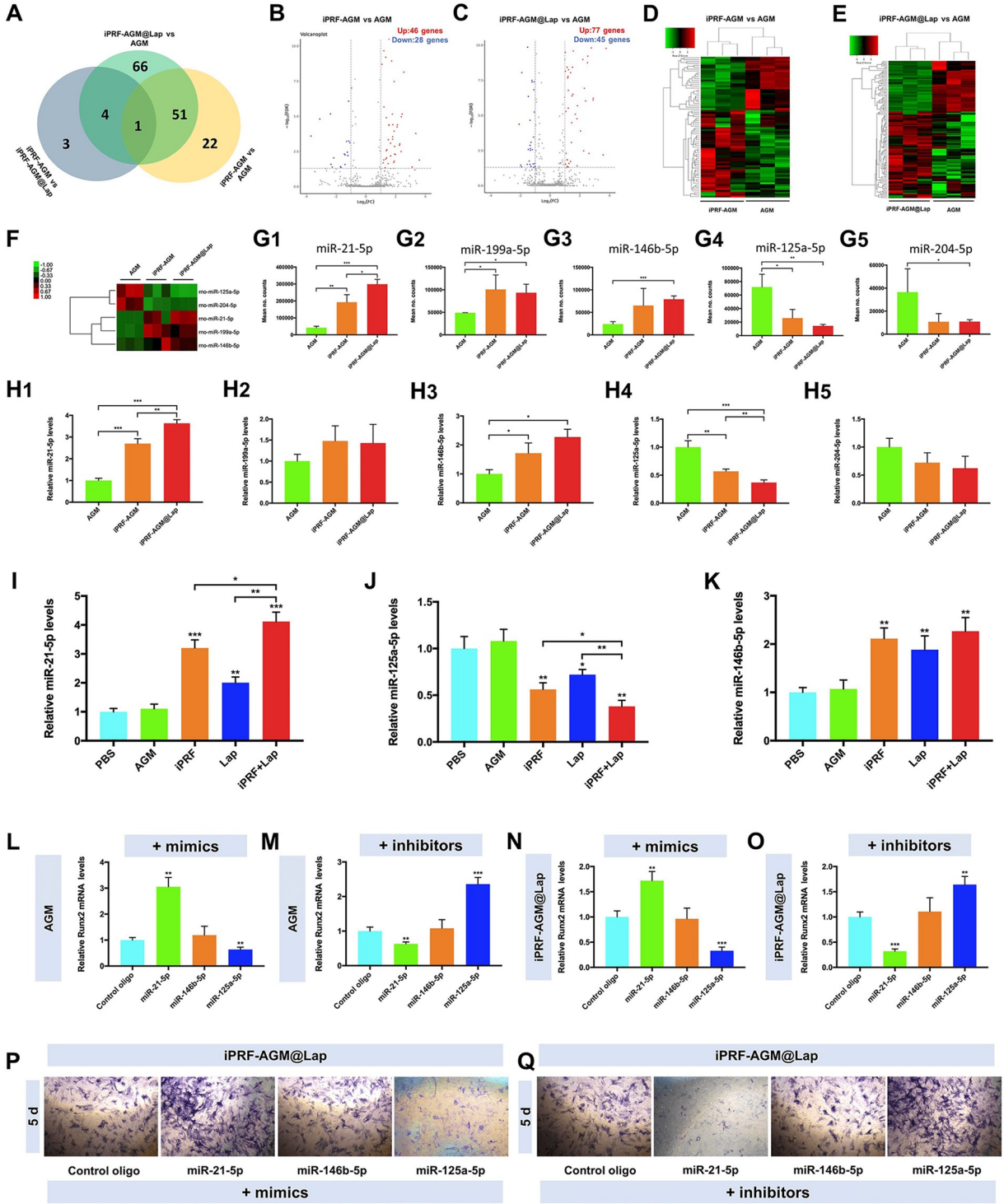

Figure 6. The i-PRF and Lap components of the scaffold synergistically regulate miRNA expression to promote BMSC osteogenic differentiation. (A) Venn diagram of the number of differentially expressed genes between groups. (B, C) Volcano plots of transcriptome analysis of differentially expressed genes. (D, E) Heat map analysis of differentially expressed genes. (F) Five candidate miRNAs significantly differentially expressed between groups. (G1–G5) Mean counts from miRNA sequencing. (H1–H5) qPCR to verify the expression of candidate miRNAs in each scaffold group. (I–K) Effects of i-PRF, Lap, and infusions of i-PRF and Lap mixtures on the expression of miR-21, miR-146b, and miR-125a in BMSC. (L, M) Effects of each miRNA mimics or inhibitors on osteogenic differentiation of BMSCs cultured on the surface of AGM scaffolds. (N, O) Effect of each miRNA mimics or inhibitor on osteogenic differentiation of BMSCs cultured on the surface of i-PRF-AGM@Lap scaffold. (O) Effect of each miRNA mimics on ALP staining of BMSC cultured on the surface of i-PRF-AGM@Lap hydrogel. (P) Effect of each miRNA inhibitor on ALP staining of BMSC cultured on the surface of i-PRF-AGM@Lap hydrogel. Statistical analyses were performed using one-way analysis of variance and Tukey's method (n = 3 independent experiments, $^{*}P < 0.05$ and $^{**}P < 0.01$). AGM, AlgMA/GelMA-methylcellulose; BMSC, bone marrow mesenchymal stem cell; i-PRF, injectable platelet-rich fibrin; Lap, laponite; q-PCR, quantitative polymerase chain reactio; ALP, alkaline phosphatase.

Figs S5 and S6, http://links.lww.com/JS9/D984). Further functional analysis of the KEGG pathway revealed that the target genes in i-PRF-AGM vs. AGM and i-PRF-AGM@Lap vs. AGM were sequentially enriched in ECM, angiogenesis, and ossification in the pro-inflammatory pathway (nuclear factor kappa-light-chain-enhancer of activated B cells (NF-κB) signaling pathway), the stem cell development and stroma formation pathway (ECM–receptor interactions and mitogen activated protein kinase (MAPK) signaling pathway), and the osteogenesis pathway (PI3K-Akt signaling pathway, hypoxia inducible factor 1 (HIF-1) pathway, and TGF-β pathway) (Supplementary Figs S7 and S8, http://links.lww.com/JS9/D984).

We selected a set of miRNAs with the highest basal expression (miR-21, miR-199a, miR-146b, miR-125a, and miR-204) and they were significantly differentially expressed in i-PRF-AGM vs. AGM and i-PRF-AGM@Lap vs. AGM in the sequencing data (Fig. 6F, G1–G5). This was subsequently validated by qPCR using sequencing independent samples, where miR-21, miR-146b, and miR-125a showed the same trend as the sequencing data (Fig. 6H1–H5). To clarify whether i-PRF and Lap could synergistically regulate the expression of the above miRNAs, we used the extracts of i-PRF, Lap, and the mixture of i-PRF and Lap to induce BMSC, respectively. qPCR assay showed that, compared with the PBS and AGM groups, i-PRF and Lap could synergistically promote the expression of miR-21 and miR-146b and inhibit the expression of miR-125a. Next, we investigated whether the above miRNAs could affect the osteogenic differentiation of BMSCs. BMSCs were transfected with miRNA mimics or inhibitors and then cultured on AGM and i-PRF-AGM@Lap gels, and it was found that miR-146b did not have a significant effect on Runx2 expression in BMSC by detecting the expression of Runx2; miR-21 mimics significantly promoted Runx2 expression in BMSC, whereas inhibition of miR-21 significantly decreased Runx2 expression; in contrast, miR-125a mimics significantly inhibited Runx2 expression in BMSC, whereas inhibition of miR-125a significantly promoted Runx2 expression. ALP staining further demonstrated that miR-21 promoted BMSC osteogenic differentiation, whereas miR-125a inhibited BMSC osteogenic differentiation.

i-PRF-AGM@Lap regulates BMSC osteogenic differentiation through miR-21- and miR-125a-mediated TGF-β/Smads signaling pathways

Further analysis of the predicted targets of miR-21 and miR-125a revealed a potential convergence of TGF-β/Smads signaling, with miR-21 and miR-125a targeting Smad 7 and Smad 4, respectively, which are key components of the TGF-β/Smads pathway.

First, the expression of key proteins in the TGF-β/Smads pathway was examined in cells cultured on each scaffold group. Western blot assay results showed that the expression of Smad 7 in the i-PRF-AGM and i-PRF-AGM@Lap groups was significantly lower than that in the AGM and blank control groups, and the expression in the i-PRF-AGM@Lap group was the lowest (Fig. 7A–E). On the contrary, the expression of Smad 4 in the i-PRF-AGM and i-PRF-AGM@Lap groups was significantly higher than that in the AGM and blank control groups, and the expression in the i-PRF-AGM@Lap group was significantly higher than that in the i-PRF-AGM group. In addition, the phosphorylation levels of Smad 2 and Smad 3 were significantly higher in the i-PRF-AGM@Lap group than in the other three groups.

Transfection of BMSCs with a miR-21 mimic significantly reduced SMAD 7 protein expression, whereas transfection of BMSCs with a miR-125a mimic significantly reduced SMAD 4 protein expression (Fig. 7F–H); conversely, inhibitors of miR-21 resulted in increased SMAD 7 protein expression, whereas inhibition of miR-125a resulted in a significant increase in SMAD 4 protein expression (Fig. 7I–K).

To further verify that SMAD 7 is a miR-21 target gene, a luciferase reporter gene containing the SMAD 7 3′-UTR carrying a wild-type or mutant miR-21-binding site was constructed, followed by transfection experiments. The results showed that the luciferase activity of the wild-type SMAD 7 3′-UTR luciferase reporter was significantly reduced with increasing doses of miR-99b mimics, whereas there was no significant change in the luciferase activity of the mutant constructs, suggesting that miR-21 regulates SMAD 7 expression through the 3′-UTR-binding site (Fig. 7L). Next, the dual-luciferase reporter assay was used to demonstrate that miR-125a can target and regulate SMAD 4 through the 3′-UTR-binding site (Fig. 7M).

Next, to further validate that miR-21 and miR-125a target Smad 7 and Smad 4, respectively, to affect BMSC osteogenic differentiation, miR-21 and Smad 7^{mut} were overexpressed in BMSC. The results showed that overexpression of miR-21 significantly promoted the expression of Runx2 and OCN, but miR-21 failed to upregulate the expression of Runx2 and OCN when Smad 7^{mut} was also overexpressed (Fig. 7N, O). Similarly, overexpression of miR-125a significantly inhibited the expression of Runx2 and OCN, but miR-125a failed to downregulate the expression of Runx2 and OCN when Smad 4^{mut} was overexpressed (Fig. 7Q, R). These results demonstrate that miR-21 and miR-125a regulate BMSC osteogenic differentiation by specifically inhibiting the expression of Smad 7 and Smad 4, respectively.

Effect of i-PRF-AGM@Lap scaffold on rat skull regeneration

To further evaluate the osteogenic properties of these scaffolds *in vivo*, a rat cranial defect model was constructed and the cranial defects were repaired using AGM, i-PRF-AGM, and i-PRF-AGM@Lap group scaffolds. None of the rats developed infection or died after scaffold implantation. Four weeks after implantation, examination of the bone defect site by micro-CT showed that the i-PRF-AGM and i-PRF-AGM@Lap groups had obvious calcification and formation of hard tissue in the cranial defect area and that the i-PRF-AGM@Lap group showed a superior repair effect, whereas no obvious new bone formation was observed in the AGM and untreated control groups (Fig. 8A). This trend was more pronounced 8 weeks after implantation when continuous new bone formation was observed in the i-PRF-AGM@Lap group from the periphery to the center of the defect area (Fig. 8B). Bone mineral density (BMD) and BV fraction (BV/TV) were further quantified using CTAn software. The results showed that the BV fraction (BV/TV) and BMD values in the i-PRF-AGM@Lap group were significantly higher than those in the blank control group and other scaffold-treated groups (Fig. 8C, D), suggesting that the newborn bone in the i-PRF-AGM@Lap group had a higher degree of bone mineralization, denser trabeculae, and, consequently, the greater load-bearing capacity. In addition, histological staining, including H&E, Masson's trichrome, and Goldner's trichrome staining, was performed on the regenerated bone 8 weeks after implantation, and representative images are shown in Fig. 8E. H&E staining showed that only a small

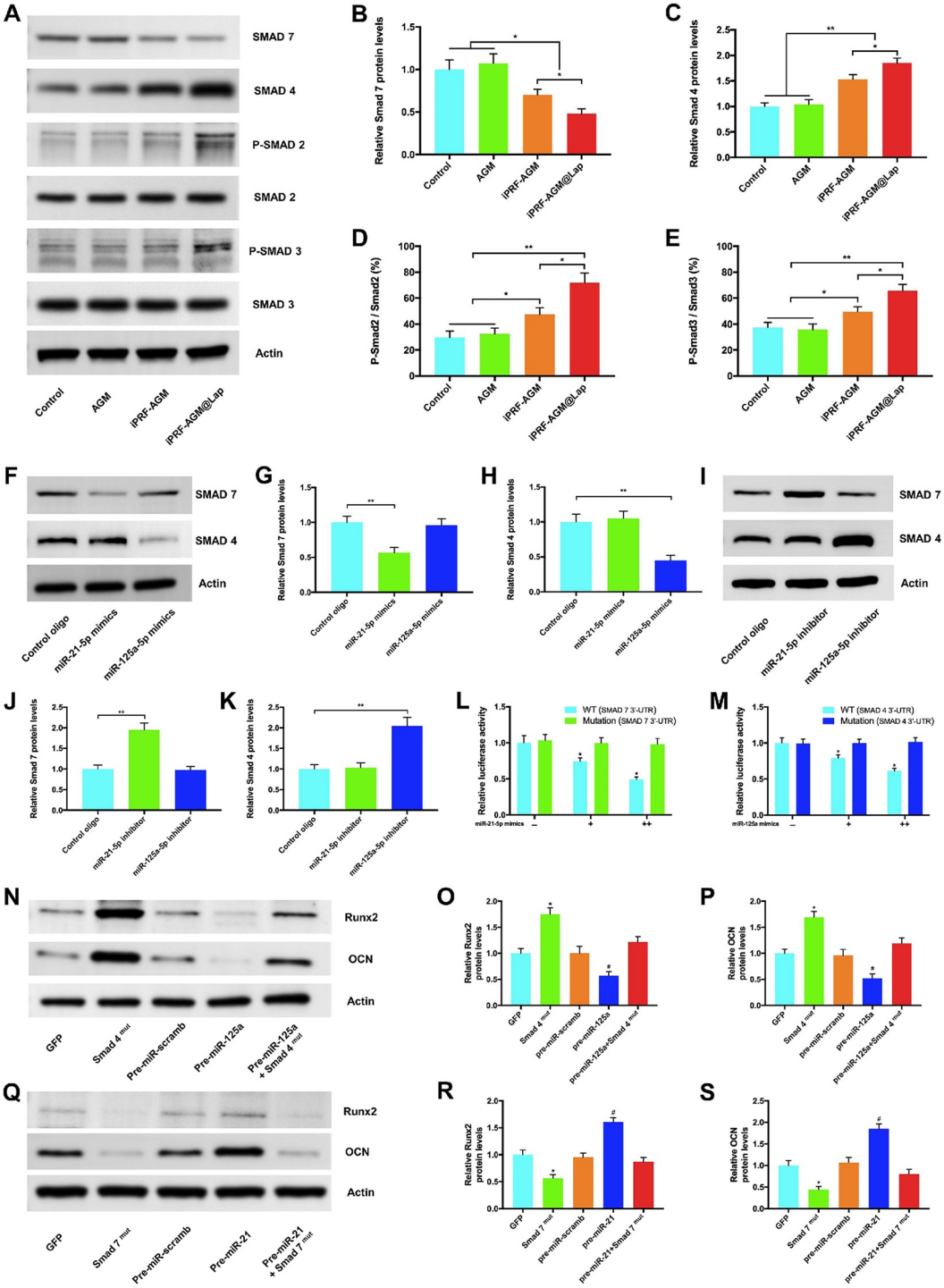

Figure 7. miR-21 and miR-125a converge on TGF-β/Smads signaling. (A) Expression of key proteins in the TGF-β/Smads pathway was detected by Western blot. (B–E) Semi-quantitative analysis of the protein expression shown in (A). (F–H) Western blot assay showed that miR-21 mimics inhibited the expression of SMAD 7, while miR-125a mimics significantly reduced the expression of SMAD 4 protein. (I–K) Western blot assay showed that miR-21 inhibitor promoted SMAD 7 expression, while miR-125a inhibitor significantly promoted SMAD 4 protein expression. (L, M) A luciferase reporter gene including SMAD 7 3′-UTR carrying WT or mutant miR-21-binding site and a luciferase reporter gene including SMAD 4 3′-UTR carrying WT or mutant miR-125a-binding site were constructed, respectively, followed by transfection experiments. The fluorescence intensity of the reporter gene was normalized to a sea kidney luciferase internal control and expressed relative to empty plasmid transfection. (N–P) Effect of pre-miR-125a, Smad 4^{mut}, and pre-miR-125a+Smad 4^{mut} on Runx2 and OCN protein expression. (Q–S) Effect of Pre-miR-21, Smad 7^{mut}, and Pre-miR-21+Smad 7^{mut} on Runx2 and OCN protein expression. Statistical analyses were performed using one-way analysis of variance and Tukey's method ($n = 3$ independent experiments, $^{*}P < 0.05$ and $^{**}P < 0.01$). AGM, AlgMA/GelMA-methylcellulose; i-PRF, injectable platelet-rich fibrin; Lap, laponite; TGF-β, transforming growth factor-β; 3′-UTR, 3′-untranslated region, wild type, W; GFP, green fluorescent protein; SMAD, suppressor of mothers against decapentaplegic; OCN, osteocalcin.

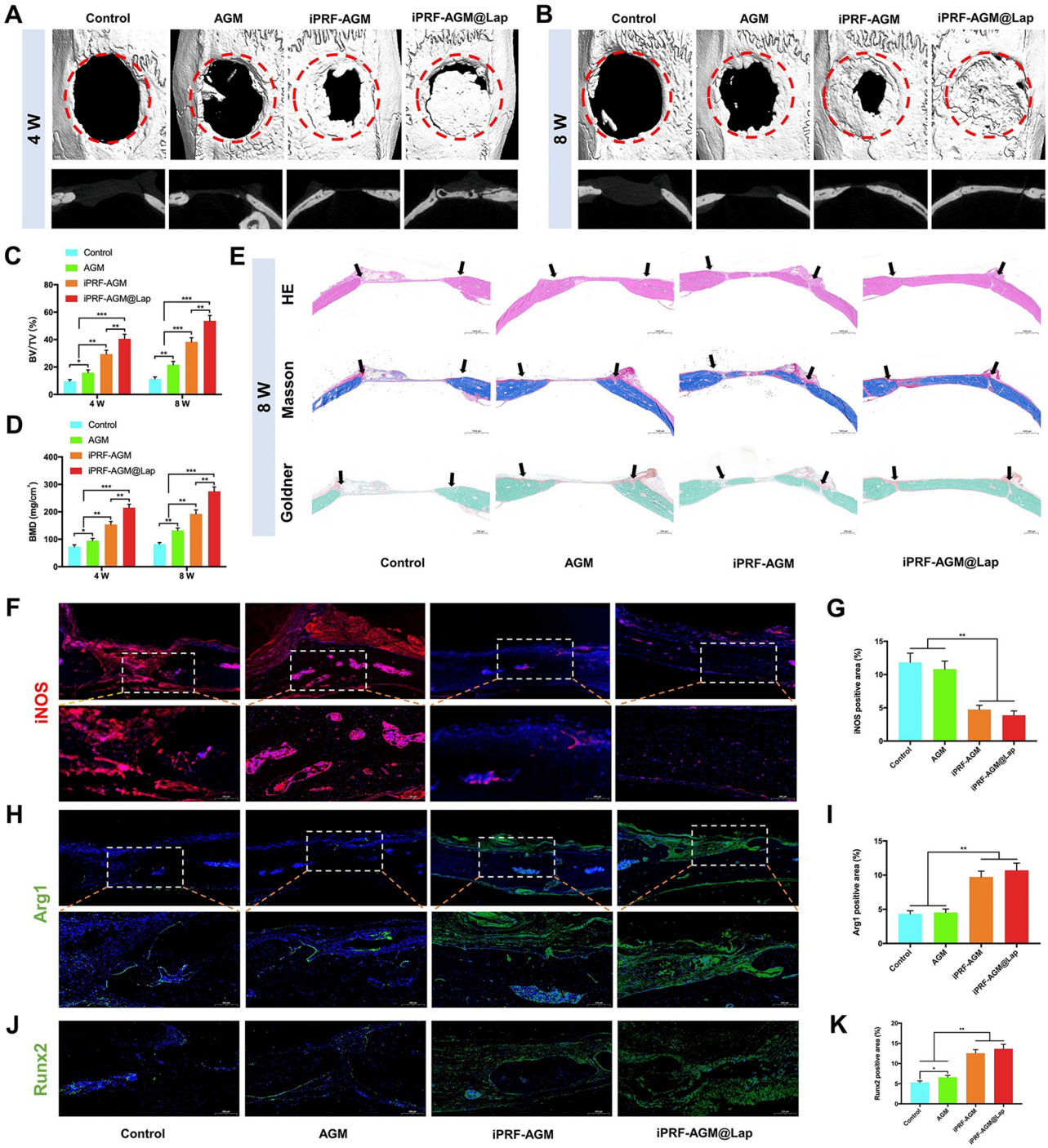

Figure 8. Effect of i-PRF-AGM@Lap scaffold on cranial bone regeneration in rats. (A) 3D reconstructed micro-CT images of the defect site 4 weeks after scaffold implantation in each group. (B) 3D reconstructed micro-CT images of the defect site 8 weeks after scaffold implantation in each group. (C, D) Quantification of bone volume to total tissue volume (BV/TV) and bone mineral density (BMD) (n = 5 per group). (E) H&E, Masson, and Goldner stained images of new bone tissue at the defect site 8 weeks after scaffold implantation, black arrows indicate the initial defect border. (F) Representative immunofluorescence images of iNOS (red) staining 8 weeks after scaffold implantation. The second row shows a higher magnification of the area within the white rectangle in the above image. (G) Quantitative analysis of iNOS-positive stained areas. (H) Representative immunofluorescence image of Arg1 (green) staining 8 weeks after scaffold implantation. (I) Quantitative analysis of Arg1-positive stained areas. (J) Representative immunofluorescence images of Runx2 (green) staining 8 weeks after scaffold implantation. (K) Quantitative analysis of Runx2-positive areas. Statistical analyses were performed using one-way analysis of variance and Tukey's method (*P < 0.05 and **P < 0.01). AGM, AlgMA/GelMA-methylcellulose; i-PRF, injectable platelet-rich fibrin; H&E, hematoxylin and eosin; Lap, laponit; iNOS, inducible nitric oxide synthase; CT, computed tomography.

amount of newly formed bone matrix appeared at the edge of the defects in the AGM and untreated control groups. Masson's trichrome staining showed only a small amount of collagen fiber formation in the AGM and blank control groups, but a large amount of collagen was observed in both the i-PRF-AGM and i-PRF-AGM@Lap groups (blue area), and in particular a small amount of mature collagen was also observed in the i-PRF-AGM@Lap group (red area). Goldner's trichrome staining also showed that a large amount of continuous mineralized bone tissue (green) was formed at the site of bone defects in the i-PRF-AGM@Lap group. Macrophages are the major functional cells involved in the immune response and associated with the repair process of bone defects, and their transition from the early pro-inflammatory M1 type to the late pro-repair M2 type plays a key role in bone regeneration[31]. Consistent with the results of *in vitro* experiments, i-PRF-AGM and i-PRF-AGM@Lap scaffolds effectively inhibit inflammation by inducing the transition of macrophages from the pro-inflammatory (M1 phenotype) stage to the anti-inflammatory (M2 phenotype) stage, thereby promoting bone defect repair (Fig. 8F–I). Immunofluorescence staining revealed that the scaffolds in the i-PRF-AGM@Lap group significantly promoted the expression of Runx2 at the bone defect site compared to the blank control group and other scaffolds, further demonstrating its excellent bone regeneration properties (Fig. 8J, H).

Discussion

We have developed a bone regeneration bioink based on i-PRF. Through the incorporation of the appropriate proportion of silicate nanoparticles, we have not only improved the printing performance of the bioink and enhanced the mechanical properties of the scaffolds but also achieved a perfect match between the functionalities of i-PRF and Lap, which has the characteristics of rapid vascularization and sustained osteogenic induction. The i-PRF-AGM@Lap scaffolds printed with this functional bioink have demonstrated strong vascularization and bone regeneration capabilities.

The encapsulation and delivery of human recombinant growth factors in tissue-engineered bone is a promising treatment for bone defects[12]. However, a number of previous clinical trials have reported adverse effects associated with these treatments[11].

The causes of these adverse effects have focused on two factors: (i) the administration of doses far in excess of the physiological dose and (ii) inappropriate delivery methods resulting in premature release[11,32].

Osteoconductive factors such as human recombinant BMP-2 and angiogenesis-stimulating factors such as VEGF have been limited in the repair of bone defects due to their high price, unstable physicochemical properties, and potential complications such as ectopic ossification and tumor formation[32,33]. Therefore, finding a safe and effective alternative to replace these growth factors and encapsulating them in 3D-printed functional scaffolds to repair bone defects are promising strategies.

Compared to single human recombinant growth factors, autologous platelet-derived biologics enriched with multiple growth factors have been widely used for tissue repair due to the advantages of easy preparation, safe source, and no immune rejection[34–36]. i-PRF is one of these platelet concentrates. As i-PRF remains liquid for approximately 20–25 min, it can be effortlessly injected and filled into tissue defect areas[13,15]. Many studies have used either simple mixing with other hydrogel materials, followed by premolding and implantation, or injection and spraying[37–39]. However, these approaches lack personalized and refinement. In contrast, 3D bioprinting introduces the advantage of "personalized printing" to the properties of i-PRF as a "personalized material" to produce scaffolds that are perfectly matched to the anatomy of the bone defect site and can be microstructurally highly bionic.

We added i-PRF into the AGM-based hydrogel precursor fluid, which was subsequently 3D printed and then formed into multi-network cross-linked hydrogel scaffolds in the presence of light curing and thrombin. However, we found that the i-PRF-AGM scaffolds were relatively weak in slowing the release of growth factors, with the majority of growth factors being released within the initial 5 days. This duration was insufficient to stimulate scaffold vascularization adequately. Additionally, we noted that, despite i-PRF's strong pro-angiogenic function, its role in promoting osteogenic differentiation was comparatively less prominent, which may be related to the fact that the functions of its released growth factors are more focused on pro-angiogenesis, and its short release time is inadequate to sustain the process of osteogenic induction. To address this limitation, the incorporation of Lap nanoparticles proved to be an effective solution. Lap not only forms strong electrostatic bonds with charged growth factors, serving as a drug delivery agent for their slow release, but it is also known for its favorable osteoinductive properties. Furthermore, Lap, as a shear thickener, enhances the shear-thinning behavior of bioinks in a concentration-dependent manner, which significantly improves the printability of bioinks. In this study, we found that the incorporation of Lap enabled the scaffold to continuously release growth factors for approximately 2 weeks, with the majority released within the initial 10 days, which was beneficial in promoting neovascularization in the early stage of bone defects. Moreover, the bioactive ions produced by Lap degradation can continue to collaborate with i-PRF to induce BMSC osteogenic differentiation continuously. The i-PRF-AGM@Lap scaffolds exhibited a slow release of Si^{4+} ions and Mg^{2+} ions for more than 40 days. Both *in vivo* and *in vitro* experiments demonstrated that the scaffolds composite with Lap exhibited enhanced bone regeneration ability, which is consistent with some previous findings[21,27,40].

Although some previous studies demonstrated the osteoinductive properties of Lap and speculated that it was related to its release of Mg^{2+}, Si^{4+}, and other ions, the specific regulatory mechanisms remain unclear. In our study, miRNA sequencing revealed significant differential expression of miR-21 and miR-125a in both i-PRF-AGM vs. AGM and i-PRF-AGM@Lap vs. AGM, with a more pronounced difference in the latter group. In order to clarify whether i-PRF and Lap could synergistically regulate the expression of these two miRNAs, we used the extracts of i-PRF, Lap, and the mixture of i-PRF and Lap to induce BMSC, respectively. qPCR assays showed that Lap and i-PRF synergistically promoted the expression of miR-21 and inhibited the expression of miR-125a, compared with those of the PBS and AGM groups. The potential convergence of TGF-β/Smads signaling was further revealed by a more in-depth analysis of the predicted targets of miR-21 and miR-125a, in which miR-21 and miR-125a target Smad 7 and Smad 4, respectively, which are key components of the TGF-β/Smads signaling pathway. The TGF-β/Smads pathway has been identified as a critical signaling pathway in the regulation

of osteogenic differentiation in BMSCs and skeletal development [41–43]. In general, signal transduction starts with ligand-induced oligomerization of serine/threonine receptor kinases and phosphorylation of cytoplasmic signal transduction molecules, where phosphorylated SMAD 2/3 binds to SMAD4 to form a complex that translocates into the nucleus. Activated SMADs can regulate a variety of different biological effects by binding to transcription factors, thereby orchestrating cell state-specific transcriptional regulation[44]. On the contrary, repressive SMADs such as Smad6 and Smad7 antagonize the activation of receptor-regulated SMADs[45]. Our study demonstrated that the i-PRF-AGM@Lap scaffold, leveraging the synergistic induction of i-PRF and Lap, regulates BMSC osteogenic differentiation through the miR-21- and miR-125a-mediated TGF-β/Smads signaling pathway.

On the other hand, as a key adsorption and delivery vehicle, the biocompatibility and long-term safety of Lap are essential to avoid harmful physiological reactions. Gaharwar et al showed that individual Lap particles were not cytotoxic below a critical concentration, with an IC50 of 4 mg/mL of Lap[46]. Veernala et al reported that Lap has a low IC50 of 2.2 mg/mL[47]. Becher et al demonstrated that the IC50 of Lap was approximately 0.5–1.5 mg/mL when cultured with HeLa or MCF-7 cells[48]. Li et al showed that concentrations of saponite as high as 10% w/v (100 mg/mL) had no effect on the viability of preosteoblastic MC3T3-E1 cells[49]. Although the short-term biocompatibility of Lap has been validated in some studies, there are few long-term safety studies related to it. Future studies need to focus on chronic inflammation and accumulation of degradation products and systematic assessment of its risks by multi-omics techniques and long-cycle animal experiments.

BMD and BV/TV affect bone strength and weight-bearing capacity from the perspectives of "bone mass" and "bone structure," respectively[50,51]. The higher the BMD, the greater the bone mineral content, and the greater the compressive and flexural strength of the bone usually is[51]. Clinically, BMD is a core indicator for the diagnosis of osteoporosis[52]. BMD mainly reflects BV and cannot fully reflect bone microstructure (e.g., trabecular connectivity and porosity). Bones with high BMD (e.g., cortical bone) are better able to withstand axial loads, but if the bone microstructure is damaged (e.g., fractured trabeculae), the weight-bearing capacity may be reduced even if the BMD is normal[52]. BV/TV refers to the ratio of bone trabecular volume to total volume and is an important parameter of bone microarchitecture, usually assessed by micro-CT or bone biopsy. Higher BV/TV results in denser and better connected bone trabeculae, which can disperse stress and reduce localized stress concentrations, significantly improving bone strength[51]. Lower BV/TV in osteoporosis results in thinner and broken trabeculae, leading to increased bone fragility (even if BMD is not significantly reduced). A trabecular network with a high BV/TV transmits loads more efficiently and plays a key role, especially in cancellous bone (e.g., vertebrae and proximal femur)[53]. In our study, we evaluated the repair effect of the scaffolds in each group by constructing a rat cranial defect model, and the results showed that the BV/TV and BMD values in the i-PRF-AGM@Lap group were significantly higher than those in the blank control group and other scaffold treated groups.

This study has some limitations and needs to be further optimized. First, we lacked long-term biocompatibility data of Lap in this study, and only small animals were used in the animal experiments of this study; medium-sized and large animal bone defect models should be added subsequently to evaluate the degradation and induction of chronic inflammation of Lap. Secondly, the lower strength of the i-PRF-AGM@Lap scaffolds, which are more suitable for repairing bone defects in nonweight-bearing bone sites such as the craniofacial region, limits their application. Follow-up studies could be conducted by injecting i-PRF-AGM@Lap bioink into 3D-printed porous PCL scaffolds with higher strength, or by intermittent layer-by-layer printing of i-PRF-AGM@Lap bioink with molten PCL bioink through a dual-channel nozzle, to construct bone repair scaffolds with high strength and bioactivity in order to validate their roles in bone defects in load-bearing bones.

The translation of tissue engineering concepts from bench to bedside is a challenging, expensive, and time-consuming process. In terms of scalable production, the transition from lab-grade 3D bioprinting to clinical-grade manufacturing will require rigorous quality control standards, including batch-to-batch consistency control, long-term monitoring of the stability of the nanoparticle–biogel interface, and assessment of the impact of growth factor activity. In terms of regulatory pathways, the composite scaffold may be categorized as a "combination product" that needs to meet the dual criteria of biomaterials and cell/tissue products, which imposes special requirements for manufacturing process validation and stability studies. From the assessment of the maturity of the technology, it is best to adopt a "stepwise transformation" strategy: first, verify the safety and efficacy in nonload-bearing bone defect models in large bone defect animals, such as pigs or sheep, then apply for ethical review of the clinical trial, and finally carry out the clinical trial of repairing traumatic craniofacial bone defects in human beings. Notably, the inter-individual variability of autologous PRF may affect product consistency, which needs to be overcome by establishing donor screening criteria or developing standardized platelet lysate substitution protocols. The establishment of an industry–university–research collaboration platform will accelerate the resolution of the above translational bottlenecks and promote the technology toward clinical utility.

Conclusion

In this study, a 3D-bioprinted i-PRF-AGM@Lap scaffold was developed for effective bone regeneration at the skull defect site in rats. i-PRF-AGM@Lap slowly releases several key growth factors produced from i-PRF, while Lap nanoparticles, a key component of the scaffold, continuously release biologically active ions, which synergistically promote osteogenic differentiation of BMSCs and significantly facilitate the vascularization process both *in vitro* and *in vivo*. In addition, i-PRF-AGM@Lap can promote macrophage M2 polarization and improve the immune microenvironment of bone. Mechanistically, we found that i-PRF-AGM@Lap could regulate BMSC osteogenic differentiation through the miR-21- and miR-125a-mediated TGF-β/Smads signaling pathway. Finally, evaluation of the rat cranial bone defect model showed that the i-PRF-AGM@Lap scaffold significantly induced bone regeneration. The results of this study provide a new idea for active biomaterial repair treatment of bone defects.

Ethical approval

All protocols involving experimental animals were approved by the Animal Welfare Ethics Committee of the Ninth People's

Hospital Affiliated to Shanghai Jiaotong University School of Medicine (SH9H-2019-A668-1).

Consent

Not applicable.

Sources of funding

The authors thank the funding support from the National Key R&D Program of China (2023YFC2507604), National Natural Science Foundation of China (NSFC: 82072421), National Natural Science Foundation of China (NSFC: 81972058), National Natural Science Foundation of China (NSFC: 81930069), Shanghai Municipal Health Commission Youth Program (2022YQ005), Basic Scientific Research Cultivation Project of Shanghai Sixth People's Hospital (ynms202104), Shanghai Jiao Tong University Medical-Industrial Crossroads Youth Project (YG2023QNA32), Technical Standard Project of Shanghai Science and Technology Commission (21DZ2201500).

Author contributions

S.Q. conceived and designed the study. B.J.C., K.Q.Z, R.T.Z., Z.Y.K., J.M.L., Z.X.K., and D.H.L. conducted the experiments. B.J.C., K.Q.Z and R.T.Z. analysed the data and wrote the manuscript. S.Q., Q.L.K. and J.X. revised the manuscript. All authors read and approved the final version.

Conflicts of interest disclosure

The authors declare that they have no competing interests.

Research registration unique identifying number (UIN)

Not applicable.

Guarantor

Shuo Qiu.

Provenance and peer review

Not commissioned, externally peer-reviewed.

Data availability statement

The data that support the findings of this study are available within the article and its supplementary materials.

References

[1] Armiento AR, Hatt LP, Sanchez Rosenberg G, *et al*. Functional biomaterials for bone regeneration: a lesson in complex biology. Adv Funct Mater 2020;30:1909874.
[2] Salhotra A, Shah HN, Levi B, *et al*. Mechanisms of bone development and repair. Nat Rev Mol Cell Biol 2020;21:696–711.
[3] Anagnostis P, Paschou SA, Goulis DG. Management of acute hip fracture. N Engl J Med 2018;378:971–72.
[4] Zhang Y, Liu X, Zeng L, *et al*. Polymer fiber scaffolds for bone and cartilage tissue engineering. Adv Funct Mater 2019;29:1903279.
[5] Zheng C, Attarilar S, Li K, *et al*. 3D-printed HA15-loaded β-tricalcium phosphate/poly (lactic-co-glycolic acid) bone tissue scaffold promotes bone regeneration in rabbit radial defects. Int J Bioprinting 2021;7:100–111.317.
[6] Zhang J, Tong D, Song H, *et al*. Osteoimmunity-regulating biomimetically hierarchical scaffold for augmented bone regeneration. Adv Mater 2022;34:2202044.
[7] Chen L, Deng C, Li J, *et al*. 3D printing of a lithium-calcium-silicate crystal bioscaffold with dual bioactivities for osteochondral interface reconstruction. Biomaterials 2019;196:138–50.
[8] Colosi C, Shin SR, Manoharan V, *et al*. Microfluidic bioprinting of heterogeneous 3D tissue constructs using low-viscosity bioink. Adv Mater 2016;28:677–84.
[9] Guo S, He C. Bioprinted scaffold remodels the neuromodulatory microenvironment for enhancing bone regeneration. Adv Funct Mater 2023;33:2304172.
[10] Freeman FE, Pitacco P, van Dommelen LHA, *et al*. 3D bioprinting spatiotemporally defined patterns of growth factors to tightly control tissue regeneration. Sci Adv 2020;6:eabb5093.
[11] Epstein NE. Complications due to the use of BMP/INFUSE in spine surgery: the evidence continues to mount. Surg Neurol Int 2013;4:S343–52.
[12] Lee K, Silva EA, Mooney DJ. Growth factor delivery-based tissue engineering: general approaches and a review of recent developments. J Royal Soc Interface 2011;8:153–70.
[13] Farshidfar N, Amiri MA, Jafarpour D, *et al*. The feasibility of injectable PRF (I-PRF) for bone tissue engineering and its application in oral and maxillofacial reconstruction: from bench to chairside. Biomater Adv 2022;134:112557.
[14] Ren S, Tang X, Liu L, *et al*. Reinforced blood-derived protein hydrogels enable dual-level regulation of bio-physiochemical microenvironments for personalized bone regeneration with remarkable enhanced efficacy. Nano Lett 2022;22:3904–13.
[15] Li N, Liu L, Wei C, *et al*. Immunomodulatory blood-derived hybrid hydrogels as multichannel microenvironment modulators for augmented bone regeneration. ACS Appl Mater Interfaces 2022;14:53523–34.
[16] Miron RJ, Fujioka-Kobayashi M, Moraschini V, *et al*. Efficacy of platelet-rich fibrin on bone formation, part 1: alveolar ridge preservation. Int J Oral Implantol 2021;14:181–94.
[17] Krishna KV, Menard-Moyon C, Verma S, *et al*. Graphene-based nanomaterials for nanobiotechnology and biomedical applications. Nanomedicine 2013;8:1669–88.
[18] Waters R, Pacelli S, Maloney R, *et al*. Stem cell secretome-rich nanoclay hydrogel: a dual action therapy for cardiovascular regeneration. Nanoscale 2016;8:7371–76.
[19] Ding X, Gao J, Wang Z, *et al*. A shear-thinning hydrogel that extends *in vivo* bioactivity of FGF2. Biomaterials 2016;111:80–89.
[20] Li S, Li Z, Yang J, *et al*. Inhibition of sympathetic activation by delivering calcium channel blockers from a 3D printed scaffold to promote bone defect repair. Adv Healthcare Mater 2022;11:2200785.
[21] Zhang Y, Xu J, Ruan YC, *et al*. Implant-derived magnesium induces local neuronal production of CGRP to improve bone-fracture healing in rats. Nat Med 2016;22:1160–69.
[22] Lee C-S, Hwang HS, Kim S, *et al*. Inspired by nature: facile design of nanoclay–organic hydrogel bone sealant with multifunctional properties for robust bone regeneration. Adv Funct Mater 2020;30:2003717.
[23] Kilkenny C, Browne WJ, Cuthill IC, *et al*. Improving bioscience research reporting: the ARRIVE Guidelines for reporting animal research. PLoS Biol 2010;8:e1000412.
[24] Cao B, Lin J, Tan J, *et al*. 3D-printed vascularized biofunctional scaffold for bone regeneration. Int J Bioprinting 2023;9:185–99.
[25] Sharma C, Dinda AK, Potdar PD, *et al*. Fabrication and characterization of novel nano-biocomposite scaffold of chitosan-gelatin-alginate-hydroxyapatite for bone tissue engineering. Mater Sci Eng C Mater Biol Appl 2016;64:416–27.
[26] Wang B, Díaz-Payno PJ, Browe DC, *et al*. Affinity-bound growth factor within sulfated interpenetrating network bioinks for bioprinting cartilaginous tissues. Acta Biomater 2021;128:130–42.
[27] Wong HM, Wu SL, Chu PK, *et al*. Low-modulus Mg/PCL hybrid bone substitute for osteoporotic fracture fixation. Biomaterials 2013;34:7016–32.
[28] Eskildsen T, Taipaleenmaki H, Stenvang J, *et al*. MicroRNA-138 regulates osteogenic differentiation of human stromal (mesenchymal) stem cells in vivo. Proc Natl Acad Sci USA 2011;108:6139–44.

[29] Schoolmeesters A, Eklund T, Leake D, *et al*. Functional profiling reveals critical role for miRNA in differentiation of human mesenchymal stem cells. PLoS One 2009;4:e5605.
[30] Frith JE, Kusuma GD, Carthew J, *et al*. Mechanically-sensitive miRNAs bias human mesenchymal stem cell fate via mTOR signalling. Nat Commun 2018;9:257.
[31] Jiang G, Li S, Yu K, *et al*. A 3D-printed PRP-GelMA hydrogel promotes osteochondral regeneration through M2 macrophage polarization in a rabbit model. Acta Biomater 2021;128:150–62.
[32] Shields LBE, Raque GH, Glassman SD, *et al*. Adverse effects associated with high-dose recombinant human bone morphogenetic protein-2 use in anterior cervical spine fusion. Spine 2006;31:542–47.
[33] Henry TD, Annex BH, McKendall GR, *et al*. Vascular endothelial growth factor in ischemia for vascular angiogenesis. Circulation 2003;107:1359–65.
[34] Wei S, Xu P, Yao Z, *et al*. A composite hydrogel with co-delivery of antimicrobial peptides and platelet-rich plasma to enhance healing of infected wounds in diabetes. Acta Biomater 2021;124:205–18.
[35] Singh M, Nanda HS, Lee JYH, *et al*. Photocurable platelet rich plasma bioadhesives. Acta Biomater. 2020;117:133–41.
[36] Oneto P, Etulain J. PRP in wound healing applications. Platelets 2021; 32:189–99.
[37] Lu G, Xu Y, Liu Q, *et al*. An instantly fixable and self-adaptive scaffold for skull regeneration by autologous stem cell recruitment and angiogenesis. Nat Commun 2022;13:2499.
[38] Feng K, Yu Y, Chen Z, *et al*. Injectable hypoxia-preconditioned cartilage progenitor cells-laden GelMA microspheres system for enhanced osteoarthritis treatment. Mater Today Bio 2023;20:100637.
[39] Zhou J, Mei J, Liu Q, *et al*. Spatiotemporal on-off immunomodulatory hydrogel targeting NLRP3 inflammasome for the treatment of biofilm-infected diabetic wounds. Adv Funct Mater 2023;33:2211811.
[40] Xie K, Wang N, Guo Y, *et al*. Additively manufactured biodegradable porous magnesium implants for elimination of implant-related infections: an *in vitro* and *in vivo* study. Bioact Mater 2022;8:140–52.
[41] Wu M, Wu S, Chen W, *et al*. The roles and regulatory mechanisms of TGF-β and BMP signaling in bone and cartilage development, homeostasis and disease. Cell Res 2024;34:101–23.
[42] Wang K, Zhou M, Zhang Y, *et al*. Fibromodulin facilitates the osteogenic effect of Masquelet's induced membrane by inhibiting the TGF-β/SMAD signaling pathway. Biomater Sci 2024;12:1898–913.
[43] Santibanez JF, Echeverria C, Millan C, Simon F. Transforming growth factor-beta superfamily regulates mesenchymal stem cell osteogenic differentiation: a microRNA linking. Acta Histochem 2023;125:152096.
[44] Thielen NGM, van der Kraan PM, van Caam APM. TGFβ/BMP signaling pathway in cartilage homeostasis. Cells 2019;8:969.
[45] Miyazawa K, Miyazono K. Regulation of TGF-β family signaling by inhibitory smads. Cold Spring Harbor Perspect Biol 2017;9:a022095.
[46] Peraro GR, Donzelli EH, Oliveira PF, *et al*. Aminofunctionalized LAPONITE® as a versatile hybrid material for chlorhexidine digluconate incorporation: cytotoxicity and antimicrobial activities. Appl Clay Sci 2020;195:105733.
[47] Wang C, Gong Z, Huang X, *et al*. An injectable heparin-Laponite hydrogel bridge FGF4 for spinal cord injury by stabilizing microtubule and improving mitochondrial function. Theranostics 2019; 9:7016–32.
[48] Kim Y-H, Yang X, Shi L, *et al*. Bisphosphonate nanoclay edge-site interactions facilitate hydrogel self-assembly and sustained growth factor localization. Nat Commun 2020;11:1365.
[49] Cross LM, Carrow JK, Ding X, *et al*. Sustained and prolonged delivery of protein therapeutics from two-dimensional nanosilicates. ACS Appl Mater Interfaces 2019;11:6741–50.
[50] Davison KS, Siminoski K, Adachi JD, *et al*. Bone strength: the whole is greater than the sum of its parts. Semin Arthritis Rheumatism 2006;36:22–31.
[51] Perilli E, Baleani M, Ohman C, *et al*. Dependence of mechanical compressive strength on local variations in micro architecture in cancellous bone of proximal human femur. J Biomech 2008;41:438–46.
[52] Siris ES, Chen YT, Abbott TA, *et al*. Bone mineral density thresholds for pharmacological intervention to prevent fractures. Archives of Internal Medicine 2004;164:1108–12.
[53] Parkinson IH, Fazzalari NL. Interrelationships between structural parameters of cancellous bone reveal accelerated structural change at low bone volume. J Bone Miner Res 2003;18:2200–05.